Theses and Dissertations   Student Graduate Works

3-23-2018

Spatial Resolution and Contrast of a Focused Diffractive Plenoptic Camera

Carlos D. Diaz

Follow this and additional works at: https://scholar.afit.edu/etd

Part of the Physics Commons

Recommended Citation

SPATIAL RESOLUTION AND CONTRAST OF A FOCUSED DIFFRACTIVE PLENOPTIC CAMERA

THESIS

Carlos D. Diaz, Captain, USAF

AFIT-ENP-MS-18-M-077

**DEPARTMENT OF THE AIR FORCE
AIR UNIVERSITY**

AIR FORCE INSTITUTE OF TECHNOLOGY

Wright-Patterson Air Force Base, Ohio

The views expressed in this thesis are those of the author and do not reflect the official policy or position of the United States Air Force, Department of Defense, or the United States Government. This material is declared a work of the U.S. Government and is not subject to copyright protection in the United States.

AFIT-ENP-MS-18-M-077

SPATIAL RESOLUTION AND CONTRAST OF A FOCUSED DIFFRACTIVE
PLENOPTIC CAMERA

THESIS

Presented to the Faculty

Department of Engineering Physics

Graduate School of Engineering and Management

Air Force Institute of Technology

Air University

Air Education and Training Command

In Partial Fulfillment of the Requirements for the

Degree of Master of Science in Applied Physics

Carlos D. Diaz, BS

Captain, USAF

March 2018

DISTRIBUTION STATEMENT A.
APPROVED FOR PUBLIC RELEASE; DISTRIBUTION UNLIMITED.

AFIT-ENP-MS-18-M-077

SPATIAL RESOLUTION AND CONTRAST OF A FOCUSED DIFFRACTIVE PLENOPTIC CAMERA

Carlos D. Diaz, BS

Captain, USAF

Committee Membership:

Lt. Col. Anthony L. Franz, PhD
Chair

Dr. Michael A. Marciniak
Member

Dr. Michael R. Hawks
Member

AFIT-ENP-MS-18-M-077

Abstract

The need for a system that would capture the spectral and spatial information of a scene in one snapshot led to the development of the conventional Diffractive Plenoptic Camera (DPC). The DPC couples an axial dispersion binary diffractive optic with plenoptic camera designs that provide snapshot spectral imaging capabilities but produce rendered images with low pixel count. A modified setup of the conventional DPC, called the focused DPC, was built and tested for the first time, and compared to the conventional DPC as a method that would produce final images with higher pixel counts and improve the quality of the rendered images. A modified imaging algorithm, the refocused light field algorithm, which would render images captured with both setups of the DPC was also programmed and tested for the first time as a method that would improve the quality of the final rendered images. The focused DPC achieved the same cutoff spatial frequency, and improved the contrast as compared to the conventional DPC in spectral regions which correlated to rendered images with high pixel count, and it shifted the wavelength at which peak performance occurred for each different case of the focused DPC. The refocused light field algorithm improved the cutoff spatial frequency of the focused DPC, and improved the contrast of both the conventional and the focused DPC setups at wavelengths far from where they had peak performance. The focused DPC was demonstrated as a system that improved performance as compared to the conventional DPC, and the refocused algorithm was demonstrated as a tool that could extend the imaging capabilities of both the conventional and the focused DPC setups.

iv

Acknowledgments

I would like to express my sincere appreciation to my faculty advisor, Lt Col Anthony Franz, and the rest of my committee members, for their guidance and support throughout the course of this thesis effort. The insight and experience was certainly appreciated. I would also like to thank my wife, my dog, and the rest of my family for giving me all the support I needed throughout the course of completing this thesis.

Carlos D. Diaz

Table of Contents

List of Figures

vii

List of Tables

INTENTIONALLY LEFT BLANK

x

SPATIAL RESOLUTION AND CONTRAST OF A FOCUSED DIFFRACTIVE PLENOPTIC CAMERA

I. Introduction

The concept of an imaging system that can capture both spatial and spectral information has existed for a while. An example of one of these imaging systems that is able to encode both location and wavelength into an image is a Fourier Transform Spectrometer (FTS)[1]. The FTS works by capturing a 2D image that captures both spatial dimensions while sweeping along a Michelson Interferometer to capture the spectral dimension, leading to a 3D image cube that has two spatial dimensions and one spectral dimensions. But the fact that the FTS needs to sweep along the spectral dimension introduces an operational time lag when operating such a system. For example, when imaging a scene that is constantly changing, such as a forest fire, this might introduce noise that might make it difficult to process the resulting images[2]. Or there could be mechanical vibrations of the instrument, referred to as pointing jitter, which adds noise considered acceptable as long as it does not exceed instrument noise[3]. Therefore, if there were a system that would be able to encode two spatial dimensions and one spectral dimension in a single snapshot, it would remove the noise that operational time lag, and the pointing jitter that the FTS introduces. The Fresnel Zone Light Field Spectral Imager[4] (FZLFSI), from here on referred to as the Diffractive Plenoptic Camera (DPC), is such a system that can capture these three dimensions in one snapshot.

1

The DPC is able to capture both spatial and spectral information in one single exposure without the need to take multiple exposures as opposed to the FTS. The DPC is able to do this by exploiting chromatic aberrations in order to create a camera that can refocus images over a broad range of wavelengths. The DPC uses a diffracting optic as its main imaging optic, known as a Fresnel Zone Plate (FZP). The FZP is a diffractive optic with the resolving power of a lens of the same diameter[5], but as opposed to regular refractive lens, the FZP's focal length depends on wavelength, which creates axial chromatic aberration (ACA)[6].
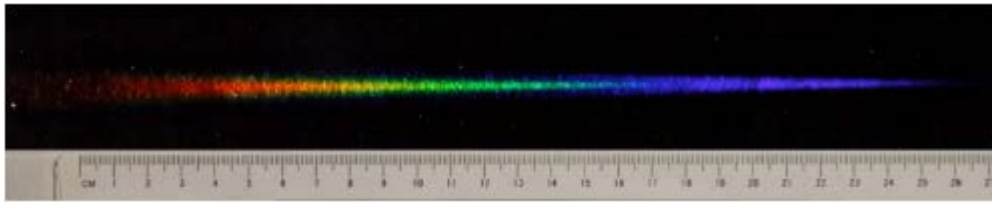
Figure 1. ACA of a diffractive optic, a Photon Sieve with a focal length of 50 cm illuminated by a white LED. This picture was taken by Will Dickinson. Image from source[7].

While the ACA introduced by a diffractive optic makes it difficult to produce an in-focus picture using a FZP, the DPC uses this effect to its advantage and creates an imaging system that is able to refocus at different wavelengths. The ACA of diffractive optics has been used for high resolution spectral imaging by translating the sensor array along the optical axis, to capture an image at different focal planes[8,9]. The DPC is able to exploit the ACA by combining an FZP with a plenoptic camera. The plenoptic camera is a concept that was introduced by Adelson and Wang in 1992[10]. It was initially introduced as a method of capturing 3D data to solve computer-vision problems and designed as a device

2

that recorded the distribution of the light rays in space, i.e., the simplified 4D plenoptic function or radiance[11].

The concept of the plenoptic camera kept evolving until 2005 when the first handheld plenoptic camera was built by Ren Ng[12,13,14]. Using his camera, Ng was able to digitally refocus across an extended depth of field from a single picture.

It was that concept of the handheld plenoptic camera that was used in building the conventional DPC, which refocuses across a spectral range instead of a depth of field. The main difference is the main imaging optic. In the case of Ng, it was a conventional refractive lens, whereas the conventional DPC used a diffractive optic, the FZP. The conventional DPC worked similar to how Ng's plenoptic camera worked, but it also suffered from some of the same setbacks that Ng's plenoptic camera suffered from. The primary setback was related to the low number of pixels in the final picture which limited the image quality.

The rendering algorithm used in both cases led to a final picture that had a drastically lower number of pixels compared to the original raw image. In Ng's case, the detector he was using had a 4,096 x 4,096 pixel array, but his final rendered images were 300 x 300 pixels. This is a reduction from a pixel count 16.7 MP to a final pixel count of 0.09 MP. The reduction in the conventional DPC was even more drastic. The original detector for the DPC had a pixel array of 5,120 x 5,120 pixel count and the final image had

3

a pixel count of 48 x 46 pixels. This is a reduction from 26.2 MP to 0.002 MP, which is a reduction by a factor of over 1000 for the overall final pixel count.

Therefore using the conventional DPC came with a price. The image could be refocused to different wavelengths which would not be possible using a standard camera, but the final images were rendered with very low pixel counts. Since this problem with plenoptic cameras has been known for a time, an alternative method had already been developed to tackle this problem.

This was known as the "full resolution light rendering"[15], from now on referred to as the focused plenoptic camera. This method, developed by Todor Georgiev and Andrew Lumsdaine in 2008, was successfully used to produce images that were refocused through an extended depth of field, but with a higher final pixel count, as compared to the method used by Ng.

It was this method that was used in conjunction with the DPC in order to make the focused DPC. Using this focused DPC, it was expected that the overall quality of the images rendered will be better than the ones rendered by the conventional DPC system.

In order to compare the two systems, a conventional DPC system and a focused DPC system were built. A target was imaged with the two systems and rendered and the final pixel count and contrast of the images compared. Of interest was the cutoff spatial frequency at each wavelength, the final pixel count and the contrast of the rendered images,

4

and the system behavior of the focused DPC at different configurations. The setup of the focused DPC allows for a range of parameters to be adjusted in order to affect the performance of the system. These different parameters were adjusted and the result in performance studied.

As a final measure of performance, a new rendering algorithm was tested. The refocusing algorithm used with the conventional DPC and the rendering algorithm used for the focused DPC are two separate algorithms that work on different principles to produce a final rendered image. A new algorithm that combines the methodology used to shift the light field in the conventional DPC algorithm and the rendering properties of the focused DPC algorithm was created and termed "refocused light field algorithm", from now on referred to as the RLA.

The rest of this work is structured in the following order: a background and theory section, an experiment section, an analysis and results section, and the conclusion and recommendation section. The background and theory section will explain the theory behind the physical components of the camera used to capture the raw images and the algorithm used to render the captured images. In this section the FZP, the conventional and focused plenoptic camera, the algorithms used in conjunction with both setups of the DPC, and the methodology used to measure the performance of these systems will be explained. Additionally the RLA will also be discussed. The experiment section describes how the DPC was set up and what optical elements were used in conjunction with the DPC in order to obtain the images that were rendered. The analysis and results section will look at the

5

rendered images, and compare them for the different cases of the DPC. This section will look at the different algorithms and setups used and understand the different situations in which a particular setup or algorithm is better suited. It also discusses the different configurations under which the focused DPC can be set and which configuration works best for different imaging scenarios that are desired. The conclusions and recommendations section will summarize the results of the experiment and will discuss what modifications can be made to the setup, or the imaging scenario in order to obtain more definite results. Furthermore, improvements to the setup and algorithm will be discussed as changes that might improve the performance of the DPC in the future.

6

II. Background and Theory

In this section the different components of the physical components of the DPC, as well as the imaging algorithms used with the DPC, will be discussed and how they work explained. Amongst these components discussed will be the FZP, and the physical components and configurations for both the conventional and focused DPC. The imaging algorithms used for both cases will be explained and discussed, and the RLA which is an amalgamation of the two previous algorithms will also be discussed, as well as a discussion on the performance metrics used in this experiment. But first, a short discussion based on geometrical optics will discuss how imaging systems work will be presented. As the DPC is an imaging system, it is important to understand how the different optical elements used in the DPC are able to image the scene presented.

2.1 Geometrical Optics Imaging

In Figure 1, it can be seen how a polychromatic source of light is spread out over a range of distances according to wavelength when using a diffractive optic along the optical axis. The range of distances over which the wavelength is spread out can be determined if one looks at the Gaussian lens equation[16]

$$\frac{1}{s_o} + \frac{1}{s_i} = \frac{1}{f}. \tag{1}$$

7

where s_o is the distance from the lens at which the object being imaged is located, s_i is the distance from the lens to the point where the image of the object will be formed, and f is the focal length of the lens being used. In the case of a refractive lens, the focal length can be assumed to be constant and the variable that changes is the distance of the object s_o, thus s_i is only a function of s_o. With a diffractive lens, such as the FZP, s_i is a function of both s_o and $f(\lambda)$. Comparing the refractive case to the diffractive case shows that building an imaging system with a diffractive optic is more complicated than it would be with a refractive optic. For a polychromatic object at a specific depth, a refractive optic would focus the entire object on the detector at the focal length of the lens, but a diffractive optic would have a certain specific color in focus while all other colors would be out of focus due to the ACA.

But if such a system were being used to image objects at a large distance, where s_o is much larger than f, then $s_i \cong f$; this case is referred to as s_o being at infinity. In a refractive lens, f is not dependent on wavelength, therefore $s_i \cong f$ is a constant, but in the diffractive optic case $s_i = f(\lambda)$ and it is not constant.

For a diffractive camera with a fixed distance between the main lens and the detector, d, it can be seen that there will be only one specific wavelength, where $s_i(\lambda) = d$, where the image will be in focus. Thus, other wavelengths aside from a "design" wavelength would appear out of focus. These other wavelengths would appear in focus if the sensor could be moved either closer to or away from the main lens, thus changing d, but in the case where the distance between the lens and the detector is fixed, that is not a

8

possibility. Therefore, if there was a way to produce focused images at these other wavelengths away from "design", it would allow for in focus images to be rendered even if they weren't captured at the design wavelength. This is the problem the DPC tackles and successfully solves as mentioned before by combining the ACA that is present in diffractive optics, such as an FZP, with the plenoptic camera.

2.2 Fresnel Zone Plate

The main imaging component in this setup is the FZP. The FZP is an object that takes advantage of what is known as the Huygens-Fresnel Principle in order to focus light. The Huygens-Fresnel principle relates to the wave nature of light and it envisions each point along the path of the wave of light to be an emitter of light itself, emitting light in all directions.

"The Huygens-Fresnel principle states that every unobstructed point of a wave front, at a given instant, serves as a source of spherical secondary wavelets (with the same frequency as that of the primary wave). The amplitude of the optical field at any point beyond is the superposition of all these wavelets (considering their amplitudes and relative phases)"[16].

9
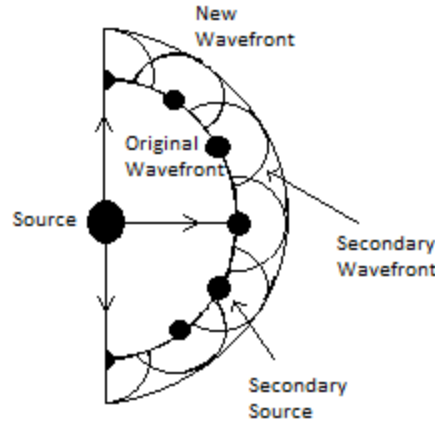
Figure 2. Secondary emissions from points in a wave. Based on image from source[17].

Figure 2 shows how these secondary wavelets add to create a new wavefront. But there is a preferred direction of propagation, because if that wasn't the case, there would be a reverse wave traveling back to the source. In order to account for this, there is a function introduced known as the obliquity factor or inclination factor, which helps describe the directionality of the secondary emissions. The obliquity factor is defined as $K(\theta) = \frac{1}{2}(1 + \cos\theta)$. It can be seen from the obliquity factor that in the forward direction, when $K(0) = 1$, this function has its maximum value, and when $K(\pi) = 0$, it has a minimum value, which indicates that the back wave dissipates.

By imagining a point source of light, such as in Figure 2, it can be seen how a spherical wave would propagate. As this wavelet propagates there will be further secondary emissions, and these would keep adding together up to another point where the secondary wavelets are added to obtain the unobstructed primary wave.

10
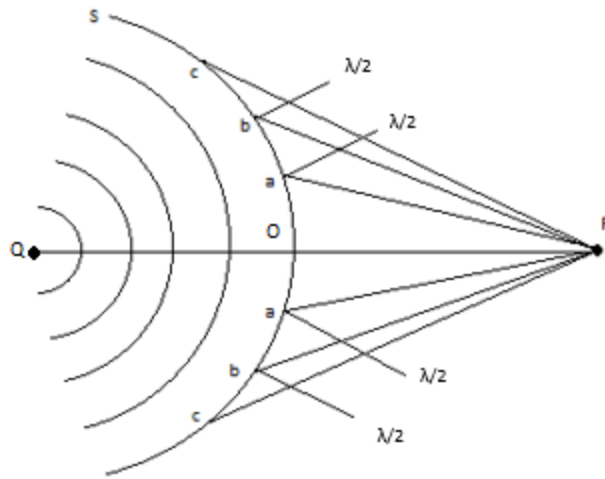
Figure 3. Spherical propagation with Fresnel Zones. Based on image from source[18].

Figure 3 shows the propagation of a spherical wavefront from point Q and it shows different points along the main wavefront a, b, and c. These three points lie on paths with half-wavelength differences in length between them. These regions that correspond to specific wavelength differences are known as Fresnel zones. According to interference, waves that are half a wavelength apart would interfere destructively, that is if they overlapped and were of equal amplitude they would cancel out. Waves that differ by a full wavelength would interfere constructively, and if they overlapped they would add together.

It is this effect that the FZP exploits in order to allow light to be focused based on wavelength. The FZP allows only the Fresnel zones in which there is a full wavelength difference between them to pass through the FZP, thus when these waves pass through the

11

FZP they interfere constructively and the observed wave is more intense. The equation that determines the focal length of the light for the FZP is given by[16],

$$f_1 = \frac{R_m^2}{m\lambda}.$$ (2)

where the R_m^2 term gives the distance from the light source to the first opening in the FZP. An FZP is designed around the value of R_m^2 so that a specific wavelength can be focused at a specific distance. In Equation 2 the m counts the Fresnel zones. This leads to values of $\frac{f_1}{3}, \frac{f_1}{5}, \frac{f_1}{7}$ and so on along the optical axis where there will be other irradiance maxima. The subscript on f_1, determines the order of the focal length, with f_1 being the first order of the focal length. For the FZP the first order contains the majority of the light being focused and will be the most intense, but due to the other orders there will be different points along the optical axis of the FZP at which light is focused but with smaller intensities. There is a special case when the focal length is zeroth order, where the light that goes through the FZP is not diffracted and not focused, but it has a smaller irradiance than the light focused by the first order. As explained previously and can be seen in Equation 2, different wavelengths will focus at different points along the optical axis, which gives rise to the ACA which the DPC uses to its advantage.

2.3 Conventional Plenoptic Camera
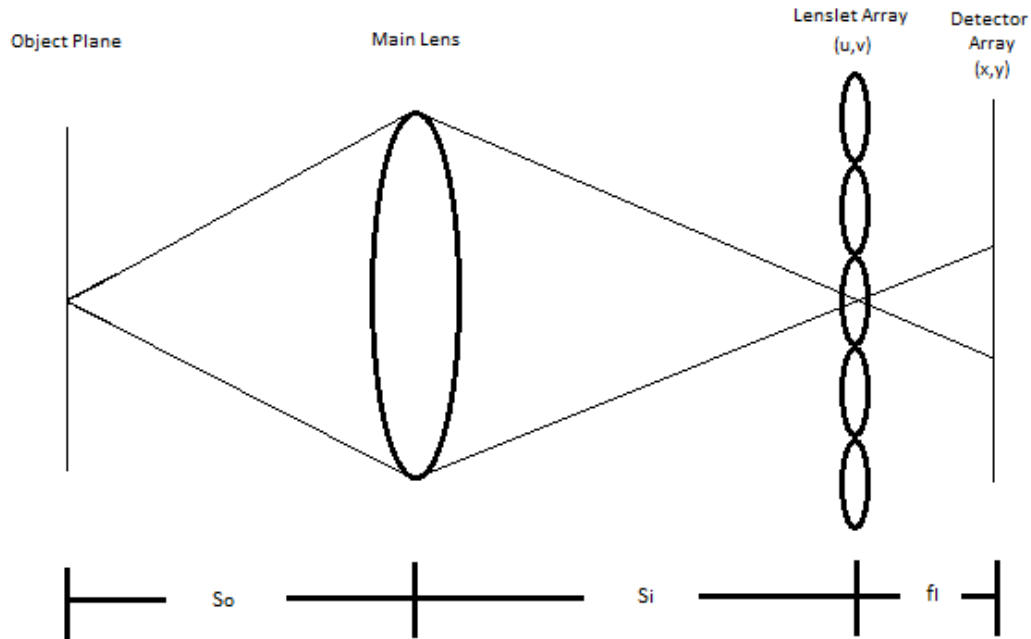
Figure 4. Internal components of a conventional plenoptic camera system. The s_o, s_i, and f_l, denote the object distance from the main lens, the image distance from the main lens, and the focal length of the lenslets respectively. Based on image from source[19].

    The three main components of the plenoptic camera as seen in Figure 4 are the main lens, the lenslet array, and the detector array. The main lens and the detector array inside the plenoptic camera function exactly like that of a conventional camera. These focus and collect the light respectively. The lenslet array differentiates a plenoptic camera from a conventional camera and allows for the collection of the full 4D radiance which can be analyzed for various purposes. The lenslet array acts as an array of micro cameras, as each of the lenslets create its own image of the scene being captured through the main lens. In

13

order to analyze the data collected by the plenoptic camera, the light field and lumigraph[20, 21] were introduced by the computer graphics community as a means of analyzing the data.

As previously mentioned, the first handheld plenoptic camera was built by Ren Ng. Ng improved upon the concept by building the handheld plenoptic camera and introducing new methods of digital processing, including refocusing[5,6,13]. With this camera, which used a refractive lens, Ng was able to digitally refocus an image to different depths, bringing objects that were out of focus into focus. This is an analog to the system mentioned above where $s_i = f(\lambda)$, but in this case $s_i = \frac{s_o * f}{s_o - f}$, where f is a constant and the only variable is s_o. Thus in his setup, Ng was able to adjust for the depth of the scene, but applying his setup to a diffractive optic, the conventional DPC is able to refocus based on wavelength if s_o is the same for all object points. But this system produces images with a low final resolution.

This issue arises from the fact that instead of producing an image with the same number of pixels as the detector of the camera, it produces an image with the number of pixels the same as the number of microlenses that are illuminated. That is to say that if the camera detector has an array of 5000 x 5000 pixels, which would correspond to a 25 megapixel camera, and the lenslet array is of 500 x 500 lenslets, the resulting image would only be 500 x 500 pixels, or 0.25 megapixels. This drastic reduction in pixel count was seen in Ng's setup, where his detector was 4096 x 4096 pixels, yet his final images were 300 x 300 pixels. For the conventional DPC the detector had 5120 x 5120 pixels, yet the

14

final images were only 48 x 46 pixels, an even more drastic reduction in pixel count. While the system suffered from this issue, it was able to produce images across a 100 nm bandwidth. Thus the DPC was proven to work, but at the cost of a sharp decrease in pixel count. But how is the conventional DPC able to refocus at different wavelengths?

This can be explained by first looking at the plenoptic function. The plenoptic function[19], $P(\theta, \varphi, \lambda, t, x, y, z)$, is a 7D function that can be thought of as carrying all the information there is to know about light in a geometrical optics setting. It doesn't carry any information about the phase of light, and the plenoptic function can be further simplified by making other assumptions, such as the function being constant in time, that light is monochromatic, and that the radiance along the ray is constant. Furthermore (θ, φ) can be replaced with Cartesian coordinates (u, v) which is done in anticipation of using these variables to represent the lenslet array coordinates. With these changes our new function can be represented as $L(u, v, x, y)$, which is commonly referred to as the lumigraph. The lumigraph is now dependent only on four spatial coordinates: (u, v) which is the plane where the light ray originates and (x, y) the plane on which the light ends at. In order to visualize how these rays travel from one plane to the other it is easier to simplify the lumigraph to two coordinates $L(u, x)$. In this scenario the coordinate in u can represent a particular point on a lens from where the light is emanating and the point in x the pixel behind the lens which the light ends on. Using this notation a coordinate in ray space can be represented by $q = (u, x)^T$. Figure 5 provides a visual representation of how these u and x coordinates can be represented in a ray-space diagram.

15
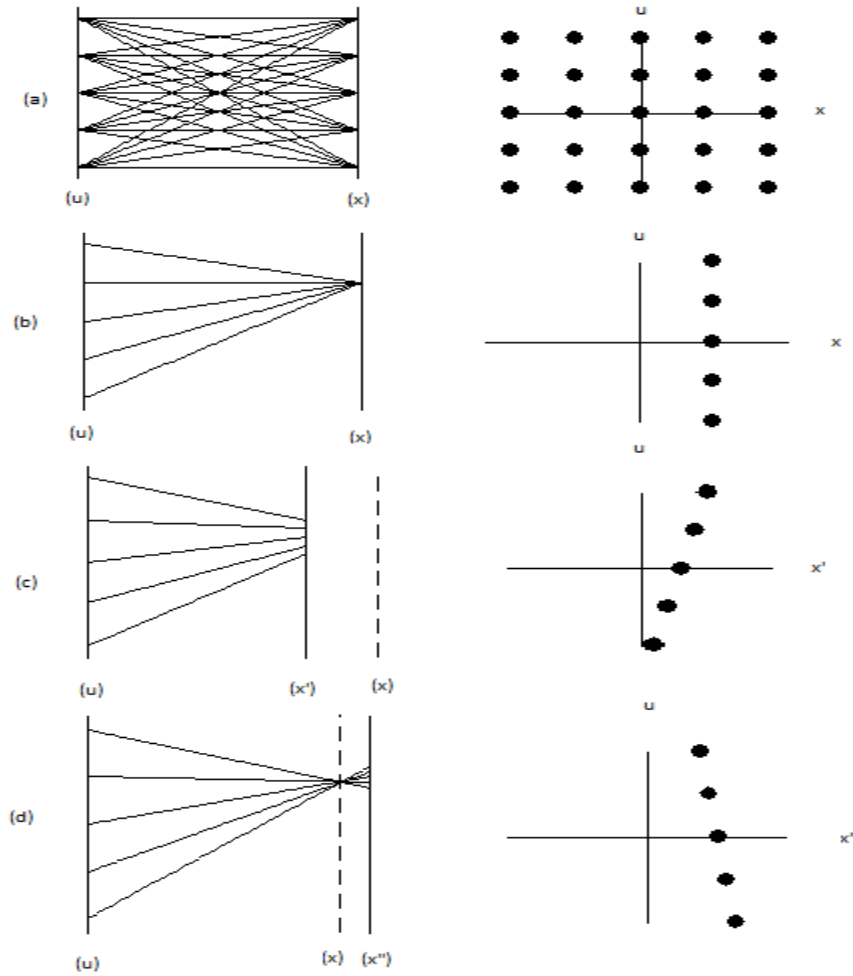
Figure 5. Illustrative plots of ray-space diagram. (a) A regular array of light rays, from a set of points in the u plane to a set of points in the x plane. (b) A set of light rays arriving at the same x position. Both (a) and (b) correspond to a detector plane that is aligned with the focal plane of the lens. (c) A set of light rays focused on a plane beyond the film plane. (d) A set of light rays focused on a plane before the film plane. Both (c) and (d) correspond to cases where the film plane does not correspond to the focal plane and there is a shift present in the (u, x) diagram. Based on image from source[19].

Figure 5 illustrates the u and x coordinates in a ray-space diagram and it does so for a two specific cases, when the film plane is at the focal plane of the lens (5(a) and 5(b)), and when it is not at the focal plane of the lens (5(c) and 5(d)). From Figure 5(b) it can be seen what would happen if a detector plane were to be placed at the x plane. For the case shown in Figure 5(b) this would lead to a captured image that is in focus. If the detector

16

plane is brought closer to the lens, as is shown in Figure 5(c), this would result in a tilt in the (u, x) plane that would result in a blurry image. The same occurs if we place the detector plane beyond the focal plane, as in Figure 5(d), where there would be a tilted line in the opposite direction as that in Figure 5(c).
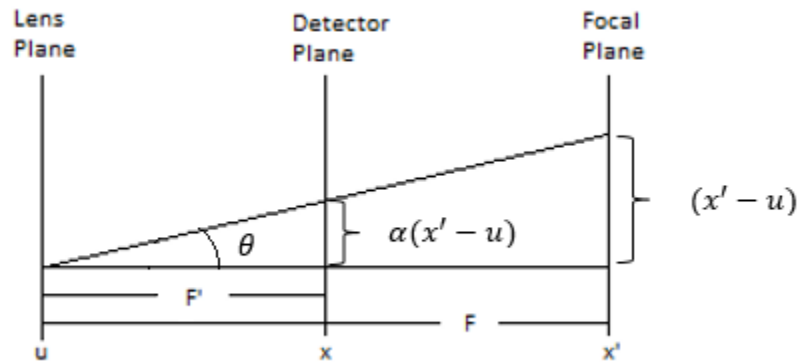
Figure 6. Ray Space coordinates showing distance between lens plane, detector plane and focal plane. The detector plane is brought closer to the lens plane by a factor that is proportional to α. Based on image in source[19].

Figure 6 shows a case similar to that presented in Figure 5(c). In Figure 6 the detector plane is placed before the focal plane of the lens and the distances between the lens plane and the detector and focal plane are denoted F' and F respectively. What is known is that if one is able to shift the detector plane to the focal plane, the (u, x) diagram would yield a straight line and the resulting image would be in focus. In order to do this one can figure out the amount that F' would need to be shifted to get to F, and that amount is given by $\alpha = \dfrac{F'}{F}$, which is the related to the amount the detector plane was shifted by

17

in Figure 6. Therefore if the position of the detector and focal plane are known the amount by which to shift the detector plane to find an image that would be in focus could be determined. But in order to be able to do this one would need to be able to capture a 4D light field, and how can one capture a 4D light field with a 2D detector array?

The answer lies in adding the lenslet array. The lenslet array adds a new set of coordinates that can be used to determine the path a light ray took through the inside of a plenoptic camera. With the lenslet array the four dimensions can be written as the (u, v) plane, where (u, v) specify the location of a specific lenslet in the lenslet array, and (x, y) plane, where (x, y) represents the location of a pixel behind a particular lenslet.

As mentioned previously the conventional plenoptic camera has a similar internal arrangement to that shown in Figure 4. The lenslet array is at the focal plane of the main lens and the detector is at the focal plane of the lenslet array.

In a conventional plenoptic camera the images are rendered from the radiance by integrating all angular samples at a particular spatial point. In the conventional plenoptic system each spatial point is given by a lenslet, and thus rendering involves adding all the pixels underneath each lenslet. As designed, rendering from the plenoptic camera only produces one pixel per lenslet which means that even with 100,000 lenslets, such as the camera built by Ng[12], produces a final image with a resolution of only 300 x 300 pixels.

18

2.4 Focused Plenoptic Camera
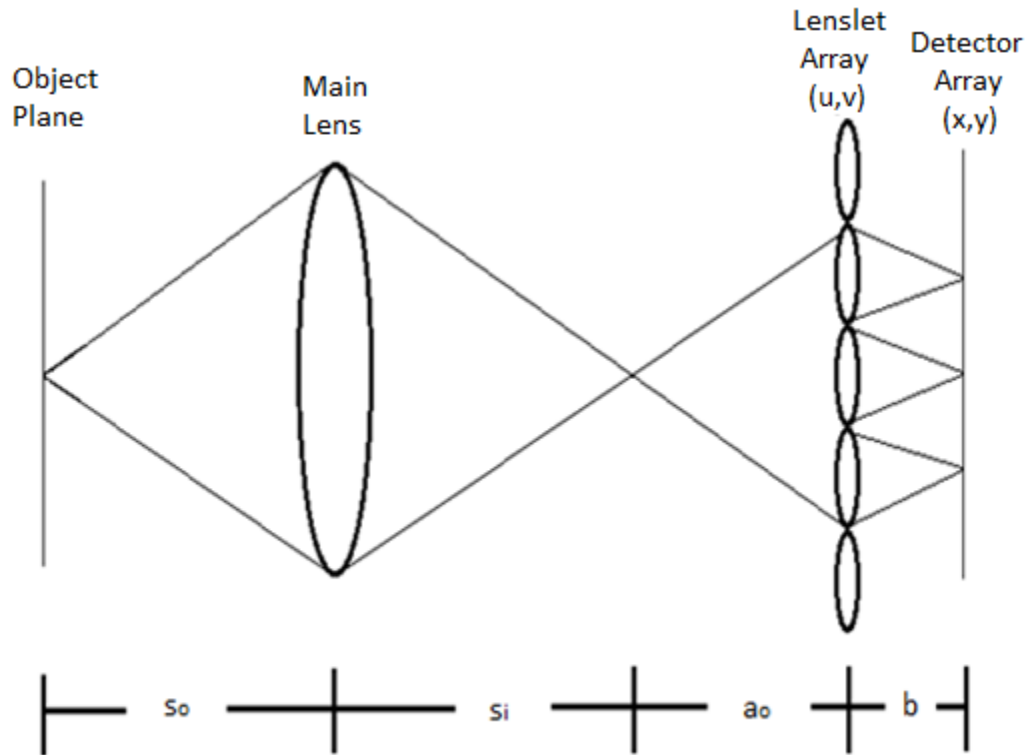
Figure 7. Internal layout for focused plenoptic camera. Based on image from source[22].

The focused plenoptic camera is different in the placing of its internal components as is shown in Figure 7. In the focused plenoptic camera the placing of the lenslet array is after the focal plane of the main lens. This means that each lenslet only captures a portion of the image formed by the main lens.

This focused approach is able to produce images with higher pixel counts based on adjusting the internal placement of the components of the plenoptic camera, which in this

paper is referred to as the focused plenoptic camera[23,24]. In the conventional plenoptic camera, the lenslet array is placed at the focal plane of the main lens and the detector array is placed at the focal plane of the lenslets. In the focused plenoptic camera, these two distances, from the main lens to the lenslet and from the lenslets to the detector array are adjustable distances that impact the overall performance of the system. Figure 5 shows these distances denoted as a_o for the distance between the focal plane of the main lens and the lenslet array, and b, the distance between the lenslet array and the detector array. The conventional plenoptic camera places the lenslet array at the focal plane of the main lens and the photodetector at the focal plane of the lenslet array.

The new focused plenoptic setup allows for a trade-off between the sampling of spatial and angular dimensions and allows positional information in the radiance to be sampled more effectively. This allows the focused plenoptic camera to produce images with higher resolutions than the conventional plenoptic camera.

This setup makes our optical system akin to a relay imaging system with the main camera lens. This setup with the lenslets satisfies Equation 1, $\frac{1}{a} + \frac{1}{b} = \frac{1}{f}$, where a, b, and f are respectively the distance from the main focal plane to the lenslet, the distance from the lenslet array to the photodetector, and f the focal length of the lenslets.

In the focused plenoptic camera the angular samples for a specific spatial point are being sampled by different lenslets. This is in contrast to the conventional plenoptic case

20

where all angular samples corresponded to a specific spatial point and thus only one lenslet. It is this fact that the focused rendering algorithm uses in order to integrate across microlens images and obtain rendered images with higher pixel counts.

This leads to the result that the spatio-angular tradeoff for the focused plenoptic camera is not constrained by the number of lenslets. In this case the optical geometry between a and b determine the spatio-angular tradeoffs. This also means that relatively large lenslets can be used to counter edge effects in the microimages.

2.5 Digital Refocusing Algorithms

Figure 6 shows what is known about an image that is out of focus and how it forms inside a camera. In Figure 6 the focal plane, F, is the location of the image, while the film plane, F', is the location of the detector plane. From the setup shown in Figure 6 it can be seen that the image captured by the camera will be out of focus. For it to be in focus, the film plane and the focal plane would have to overlap. But if the distance to the film plane, F', and the distance to the focal plane, F, are known, then the amount that F' has to be shifted to bring it to F is already known. This quantity is related to the α term and it is given by $\frac{F'}{F}$. This quantity, α, will inform on how much the F' plane needs to be shifted in order to obtain an image that is in focus, and that will be used in the conventional algorithm in order to refocus the image.

21

For the conventional case the digital algorithm works in a series of steps. The first step is to make the 4D light field out of the 2D raw image.
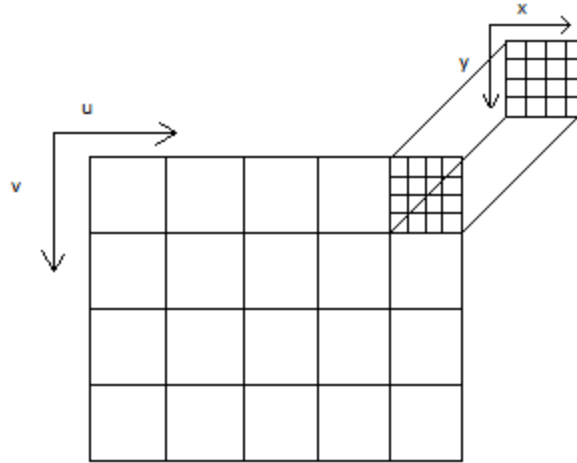
Figure 8. Position major "microlens images" created from the raw image. Based on image from source[24]

Figure 8 shows how the "microlens images" are created from the raw image. Each microlens image is built by creating a 2D array of all the pixels that are underneath each lenslet. This method creates a 2D array for each lenslet, from the 2D array of the entire raw image, which in turn gives rise to the 4D array that is the resultant light field. Two of those dimensions (u, v) give the position of the lensets, and the other two dimensions (x, y) give the position of the pixel behind the lenslet. This type of array that is built is a "position major". This is because every microlens image corresponds to a different position in the overall scene.

22
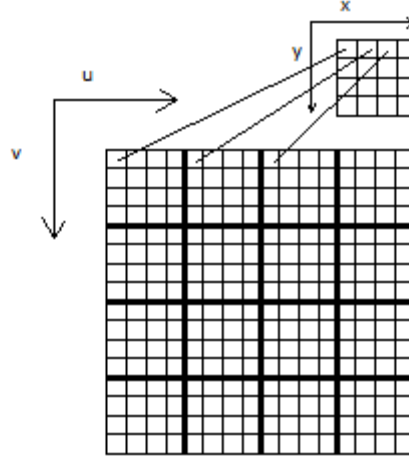
Figure 9. Direction major "sub-aperture images" created from the raw image. Based on image from source[24].

Figure 9 shows how the other type of 4D array, the "direction major" array, is built. Like the position major, the direction major is a 4D light field array but it is built differently. Since there is a difference in the way the array is built and the type of information each separate 2D array shows, the images formed by 2D array is termed "sub-aperture image" instead of "microlens image". Instead of building a microlens image by taking all the pixels underneath a lenslet, the direction major makes a sub-aperture image by taking all the pixels corresponding to a specific (x, y) value underneath each lens and creating 2D arrays that all correspond to specific pixels underneath every lenslet. Each sub-aperture image built in this fashion shows the same scene but from a different perspective or direction. It is with this setup that the digital refocusing can be done.

23

With the direction major 4D array, the second step is to shift each sub-aperture image the required amount. The shift that is required for each sub-aperture image is given by $u(1 - \frac{1}{\alpha})$ in the x direction and by $v(1 - \frac{1}{\alpha})$ in the y direction. Once each sub-aperture image, is shifted each individual pixel corresponding to a specific (x, y) coordinate from every sub-aperture image is added to create the overall shifted image. The resulting image is the scene focused on the depth given by F'.

In the setup being used in the experiment, the shift was given by the wavelength, thus $\alpha(\lambda) = \frac{F'(\lambda)}{F}$. With this setup the final rendered image has one pixel per lenslet, leading to the low resolution problem encountered with the conventional algorithm.

The other algorithm used in this experiment is for the focused DPC. The focused algorithm makes use of the position major 4D array in order to make the rendered imaged.
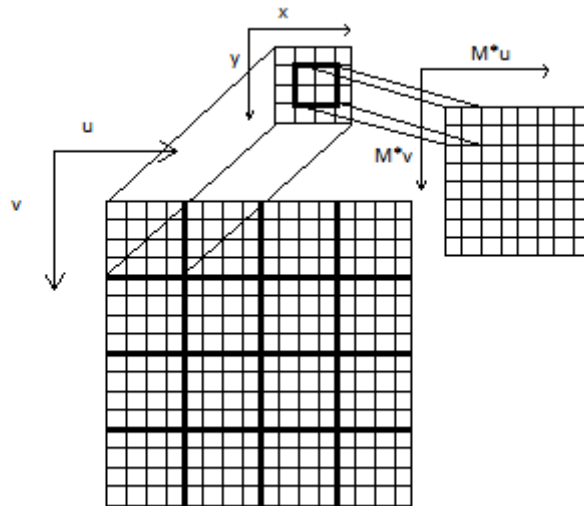
Figure 5. Process of rendering an image with the focused algorithm. Based on image from source[24].

24

Figure 10 shows the process by which the focused algorithm makes an image. The focused algorithm takes the "position major" 4D array and takes a patch of pixels from each one of the microlens images. This patch of pixels is placed into the corresponding position in the new image. A patch of pixels is taken from each microlens image to construct the overall rendered image which will have a total pixel count of $(M \times u) \times (M \times v)$, where M is the patch size used in the algorithm, and u and v are the number of lenslets in the horizontal and vertical direction respectively. It is important to note that changing the area of the microlens image from where the patch of pixels is grabbed changes the perspective of the overall scene rendered. This can be best explained by looking at Figure 11.
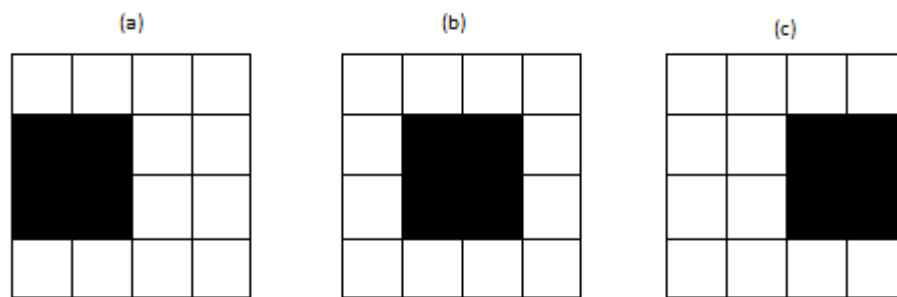
Figure 11. Patch size of two being collected from different pixels in a microlens image. Based on image from source[24].

Figure 11 shows a patch size of two being collected from a 4x4 microlens image, but each has the patch being collected from different areas of the 2D array. The rendered images that will be produced by grabbing the patch from the different areas will result in

www.manaraa.com

the same scene but from different directions. This is important because it ties into how the images rendered in the experiment using the focused algorithm are made.
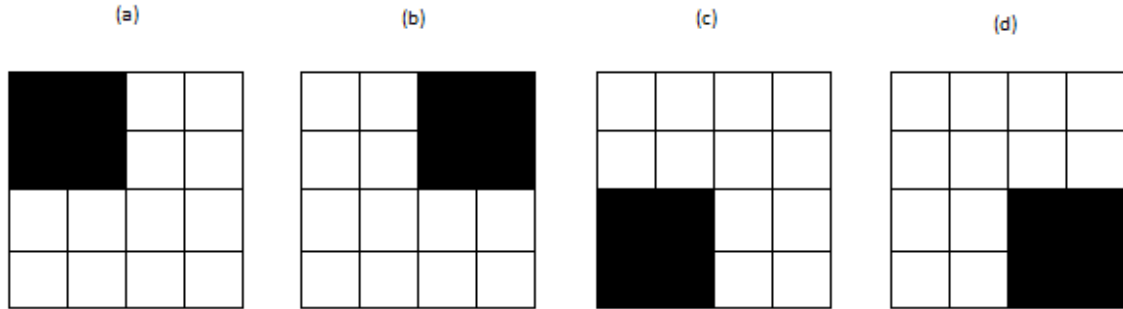
Figure 12. Rendering of the same microlens image from different perspectives. Based on image from source[24].

Figure 12 shows four different cases, where each one has the same patch size grabbed from a different part of the array. These successive patches iterate through the 2D array in such a way that it images the whole array. Each one of the cases will produce a rendered image of the scene from a different perspective with a number of pixels given by $(M\ x\ u)\ x\ (M\ x\ v)$. The algorithm will produce an image that has $(M\ x\ u)\ x\ (M\ x\ v)$ pixels from every direction, and the produced will take all these images that were rendered from these different perspectives and add them on top of each other.

The patch size M, to be used with the focused algorithm, can be determined by relating the amount of pixels that are being illuminated to the transverse magnification of the lenslet which can be calculated in two ways[8].

26

$$M_T = -\frac{s_i}{s_o}, M_T \equiv \frac{y_i}{y_o} \qquad (3)$$

Equation 3 is the transverse magnification provided by a lens and as shown can be calculated in two ways. If M_T is negative the image is inverted and if it is positive it stays in the same orientation. The first method relates the transverse magnification to the object and image distance, s_o and s_i respectively, which in the focused plenoptic setup are a and b respectively. The second method relates to the size of the object and the size of the image, which are given by y_o and y_i respectively. In the focused plenoptic case, each lenslet only images a portion of the scene, and this portion is corresponds to a height of the image plane that is almost equal to the height of the lenslet. This means that $y_o = \mu$, where μ is the size of the lenslet. This gives the height behind the lenslet that will be illuminated, and is given by $y_i = -\frac{b*\mu}{a}$. This quantity, which has units of length, can be divided by the size of the pixels, s, to give an estimate of the number of pixels that will be illuminated for a certain a, b, and μ[15].

$$M(\lambda) = \frac{\mu*b}{a(\lambda)*s} \qquad (4)$$

In Equation 4 the M gives us the number of pixels that would be illuminated for different values of $a(\lambda)$. This equation will be used to determine the value of M to use when rendering the final image with the focused algorithm. In the setup for the experiment the a is wavelength dependent, thus we have $a(\lambda)$ in Equation 4. The b that is shown in

27

Equation 4 is a fixed value that is determined by Equation 1 for a design wavelength. In order to find the value of b, a physical distance between the focal plane and the lenslet plane is established at a specific wavelength, in this experiment 770 nm, and this distance is termed a_o and is related to b via the following relation $b = \frac{a_o * f}{a_o - f}$, where f is the focal length of the lenslets. This value of b is the physical distance between the lenslet array and the detector. This value of a_o is used to determine b and can be positive or negative depending on whether the lenslet array is placed before or after the focal plane of the detector at the design wavelength. There can only be positive values of b, as b denotes the distance between the lenslet array and the camera. This value of a_o also affects the value of $a(\lambda)$ that is used in Equation 4 via the following relation,

$$a(\lambda) = s_i(770\ nm) + a_o - \frac{s_o * f(\lambda)}{s_o - f(\lambda)} \tag{5}$$

where $s_i(770\ nm)$ is the distance to the image plane from the main lens at the design wavelength, s_o, is the object distance, and $f(\lambda)$, is the focal length of the imaging optic which is dependent on the wavelength of the incoming light. Large values of M produce images with high pixel count, and we expect these images with high pixel count to be some of the best resolved images that are produced. Knowing the dependence of b, $a(\lambda)$, and $M(\lambda)$ on these values, it is possible to plot $M(\lambda)$ vs λ. These plots will help shed light on some of the results presented in the Results & Analysis section.

28
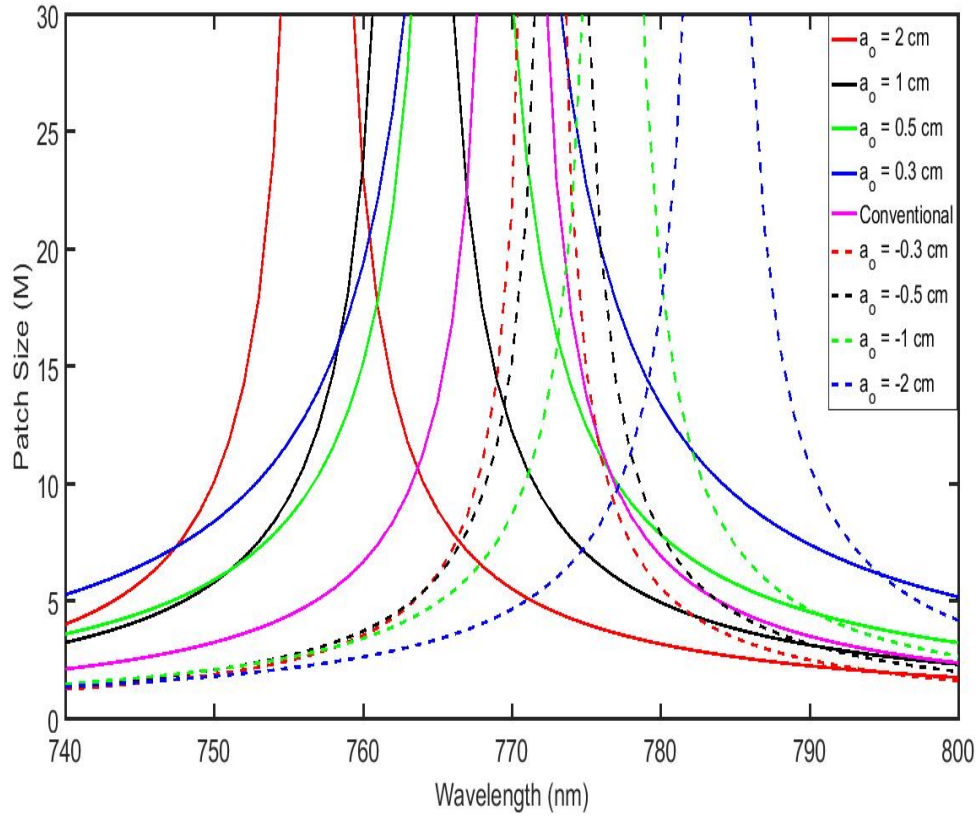
Figure 6. Patch size versus wavelength plot for different values of a_o. It can be seen that as a_o, goes from negative to positive values the plotted curve moves from lesser to greater wavelengths, with the conventional setup, $a_o = 0$, centered around the design wavelength. The central maximum for each of these curves correlate to areas with the highest spectral frequency content imaged for each of the different setups. The values of a_o for which these curves were plotted were the values of a_o used in the experiment, and the range of wavelength for which the curves are plotted correspond to wavelengths which were imaged in the experiment. The values of μ and s used also correspond to the physical setup used in the experiment.

As can be seen in Figure 13, the value of a_o, affects the positioning of the M curve

relative to the central wavelength of $\lambda = 770$ nm. Looking at Equation 4 it can be seen

that the peak of each one of these M curves correspond to a value of $a(\lambda) = 0$. Looking at

Equation 5, rearranging the terms, and substituting in $f(\lambda) = 50 \frac{800*10^{-7}}{\lambda}$ cm, a relation for

the wavelength which corresponds to this zero value of $a(\lambda)$ can be obtained, $\lambda = 50 *$

29

$800 * 10^{-7}(\frac{1}{s_i(770\ nm)+a_o} + \frac{1}{s_o})$ cm. For the values of a_o, μ, b, and s that were chosen in the experiment the central wavelength for each a_o correspond to the values shown below.

Setup	Wavelength
$a_o = -2$ cm	783.8 nm
$a_o = -1$ cm	776.8 nm
$a_o = -0.5$ cm	773.4 nm
$a_o = -0.3$ cm	772.0 nm
$a_o = 0$ cm	770.0 nm
$a_o = 0.3$ cm	768.0 nm
$a_o = 0.5$ cm	766.7 nm
$a_o = 1$ cm	763.4 nm
$a_o = 2$ cm	756.9 nm

Table 1. Central Wavelength corresponding to each value of a_o. Similar to Figure 13, each negative values of a_o is centered on a wavelengths greater than design, and for positive values of a_o, they are centered at wavelengths less than design.

Table 1 shows a similar pattern to that seen in Figure 13, where negative values of a_o have central wavelengths at values greater than design, and positive a_o have central wavelengths at values less than design. Near these centers the patch size is large, sometimes larger than what is physically achievable with the system. These large patch sizes correspond to rendered images with a much higher pixel count than those rendered with

30

the conventional setup, and they also overlap with areas that the system is imaging near the image plane. Therefore these new central wavelengths for each system should correspond to an area where the focused plenoptic system operates at its best, and it will be seen that there is strong correlation between the central wavelength and the performance of the focused DPC.

The advantages and disadvantages of both of these configurations, the conventional plenoptic and the focused plenoptic, are already well known and were tested in this experiment. For the conventional algorithm the depth of field, or the spectral range in our case, through which the image can be refocused is a maximum but the rendered images have a very low pixel count. For the focused algorithm the rendered images have a higher resolution, but the spectral range through which these images can be rendered is narrower. Thus with either choice there is an option, and that is whether the need is a system with a very broad spectral range with poor image resolution, or a narrow spectral range with higher pixel count. As was mentioned before both algorithms work by different methods. The conventional algorithm works by shifting each individual sub-aperture image from the direction major 4D array and then adds these images together. The focusing algorithm works by grabbing a patch of pixels from each microlens image from the position major 4D array and putting these together to make a rendered image. Due to the fact that the 4D array in the focused algorithm case is not shifted this leads to the narrower range through which the focused algorithm will produce an in focus image. But if the 4D array is shifted according to the conventional algorithm, and then the shifted 4D array is rendered using

31

the focused algorithm, would this both improve the range and the resolution of the rendered images?

This is termed the "refocused light field algorithm", or RLA, and it was tested with both images taken by the conventional and the refocused DPC setup. The RLA works by first creating the direction major 4D array from the raw image and shifting it according to the principles of the refocusing algorithm used with the conventional setup. Once the direction major 4D array is shifted, it is transformed in to a position major 4D array. This position major 4D array is then rendered using the focused rendering algorithm which results in an image with a higher pixel count that is also refocused.

2.6 Cutoff Spatial Resolution and Contrast
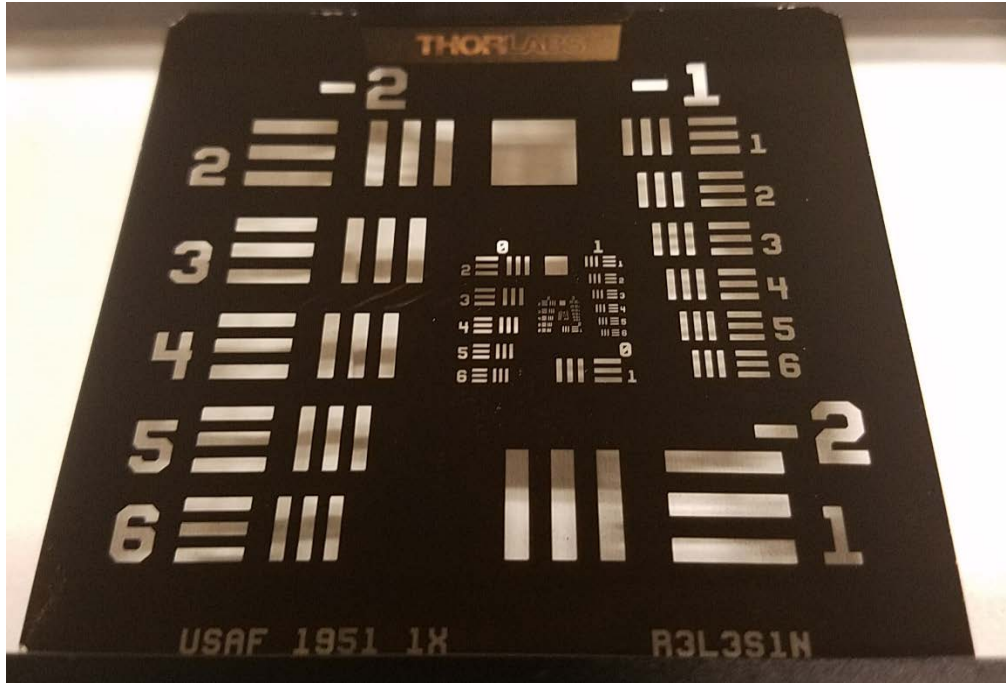
Figure 7. 1951 USAF Resolution Target used in experiment

The two metrics of performance that were applied to the system were the spatial cutoff frequency of the system and the contrast of the rendered images. Due to the nature of the target being imaged, a 1951 USAF Resolution Target, these metric were applied as a means to calculate performance.

The cutoff spatial frequency measurement relates to what is the smallest spatial frequency that the system could resolve at different settings and wavelengths. This would be determined by noting what was the smallest element that could be resolved from the

33

1951 USAF Resolution Target. In order to convert from the smallest element resolved to a spatial frequency, the following equations were used[25]

$$R = 2^{k+\frac{N-1}{6}} \ , \qquad R_A = R * f_c \qquad (6)$$

where R is the resolution at the target, in lines/mm, k is the group number, N is the element number, R_A is the spatial resolution in cycles/milliradians and f_c is the distance from the target to the imaging optic in meters. Equation 6 is what allows the USAF Resolution Target to be expressed in units of cycles/milliradians and it is what was used to determine the cutoff spatial frequencies shown later in this document.

The next measuring criteria examined were contrast measurements which are normally done on an image which has neighboring areas with different intensities. As can be seen in Figure 16, the target has many areas where this is applicable, as it has bars where the light goes through, and it appears bright on an image, and in between those bars it has blocked off areas which in principle should result in a dark area in an image. The contrast can be calculated according to the following equation[16],

$$C = \frac{I_{max} - I_{min}}{I_{max} + I_{min}} \qquad (7)$$

where I_{max}, is the value of the intensity at the illuminated area, or at the max illumination, and I_{min} is the value of the intensity at the dark area, or the minimum illumination. Using this method and the nature of the rows and columns present in each element of the 1951 USAF Resolution Target, there were eight values of contrast that could be calculated for each element. These eight values corresponded to four values calculated from the

34

horizontal bars, the rows, and four calculated from the vertical bars, the columns. These four values were calculated by estimating the maximum intensity at the three slits for either the rows or columns, and estimating the minimum intensity at the two dark regions in between the three slits for either the row or the columns. With this there were a total of five values that were obtained for both the rows and the columns. From these five values the first maximum intensity and the first minimum intensity where used to get one estimate for the contrast. Then the first minimum intensity and the second maximum intensity where used for a second calculation, followed by the second maximum again, but now in comparison for the second minimum for a third calculation. The fourth value was calculated from the second minimum and the third maximum, which yielded a total of four values for the rows and four more values for the columns.

III. Experiment

This section will explain the physical setup of the experiment and the components used in the experiment. It will illustrate how the system was setup and what distances were placed between the objects in order to achieve the ideal imaging conditions. The uncertainties with several of the instruments used will also be discussed, as well as the values of a_o and b that were used in the experiment along with the uncertainty associated with those values.

The components used for the experiment were the light source, a spatial filter, a lens that collimated the beam, the target, the FZP, the lenslet array, and the board camera.
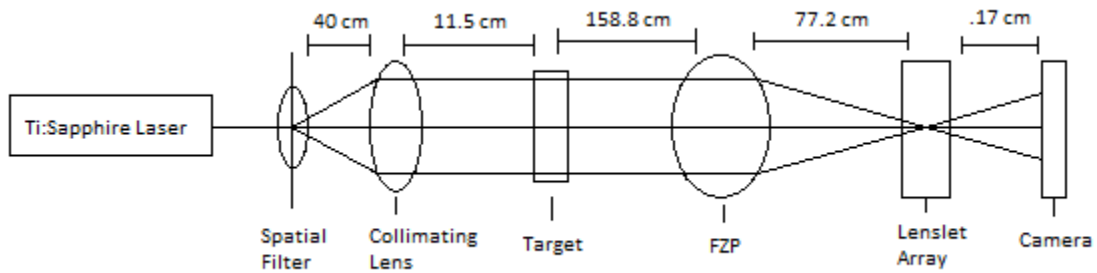
Figure 8. Setup used for experiment with the distances being shown for the design wavelength.

Figure 15 shows the order of the setup and the distances between each successive element. Between the Ti:Sapphire laser and the spatial filter there were two flat mirrors used to guide the beam, but the rest of the components that were present in the experiment

36

are shown in Figure 15. The distances shown between the FZP and the lenslet array, and the lenslet array and the camera are those of the system at the conventional setup. For the focused setup these distances are varied to obtain different results.

The light source used in the experiment was a Spectra-Physics 3900S, continuous wave (CW), Ti:Sapphire Laser that had a tunable range from 700 – 1000 nm. The cavity optics that was used during the experiment allowed for the laser to be tuned from 700 – 850 nm. The cavity of the laser uses a birefringent filter that allows for the selection of a narrow frequency bandwidth to pass through it, and continue through the cavity. It is the tuning of this birefringent filter that allows for the selection of a specific wavelength to be emitted from the laser. An Exemplar spectrometer (BRC115 P-V-VIS/NIR) with a range of 300-1000 nm and a resolution of 0.98 nm at 546.17 nm was the tool used to determine the wavelength being emitted by the laser. In this report[26] the uncertainty of this device was determined to be ±0.4 nm.

The next item in the path of the beam is the spatial filter. The spatial filter helps remove some of the aberrations present in the laser beam introduced by any imperfections in the cavity. The spatial filter consisted of a 20x microscope objective and a 25 μm pinhole. The pinhole was placed at the transform plane of the microscope objective and it would only allow the central bright spot of the observed Airy pattern to be transmitted. This removed the higher spatial frequencies present in the beam, and cleaned up the beam.

The lens was placed after the spatial filter serves to collimate the point source and the collimated light from this lens was used to image the target. The lens has a focal length of 40 cm and it was originally designed to collimate the target but there was a complication. The image of the point source was being focused right before the target was imaged, therefore creating a bright spot in the middle of the image. The target could be imaged without complication by having the spatial filter collimated and having the target within less than a focal length of the lens, and this was the design that was used throughout the imaging process.

Figure 14 shows the 1951 USAF Resolution Target, which was located right after the collimating lens. The resolution target has a repeating pattern that decreases in size as the index increases. This variability in size and the ability to choose a different sized set of bars to image was the deciding factor in using the resolution target as the object to be imaged. The organization of the bar chart is done via groups and elements. The elements are the repeating rows and columns numerated from 1 to 6, and the group denotes the size of the elements underneath.

The next item was the FZP itself. The FZP had a focal length of 50 cm at a design wavelength of 800 nm. Since the laser had a tunable range from 700 – 850 nm, it was decided that the center wavelength would be 770 nm, which would correspond to a focal length of 51.94 cm at this wavelength. Due to the fact that the light coming from the target was not collimated, the lenslet array could not be placed at this distance in order to image the target. The image plane of the target at a wavelength of 770 nm was at a distance of

38

77.2 cm away from the FZP. This wavelength, 770 nm, was chosen to be the center wavelength because it would allow for an equal amount of shift in either increasing or decreasing the wavelength. But if a different wavelength would be desired as the center wavelength with the same setup, the only change that would need to be made is to adjust the distance between the lenslet array and the FZP. Although not explored in this experiment, this presents some flexibility in the design of the DPC as it allows a central wavelength to be chosen, which might be chosen based on experimental constraints or on imaging considerations.

The lenslet array used in the experiments had 100 x 100 μm lenslets with a focal length of 1.7 mm, and an f-number of f/17. The f-number of the FZP is 16.6 which matches closely to that of the lenslets, which is desirable[6]. Lenslet arrays with lenslet sizes of 200 x 200 μm, and 500 x 500 μm were also tested but these did not produce favorable results. The reason why these did not produce favorable results was because the refocused image produced by the conventional algorithm creates an image with one pixel per lenslet in the final image. For both the 200 x 200 μm and 500 x 500 μm size lenslets the final images produced had very low pixel counts and these images were not discernible. The lenslets used in the experiment were manufactured by RPC Photonics.

The camera used in the experiment was the DMM 27UJ003-ML board camera manufactured by Imaging Source. This camera had a total pixel count of 3,856 x 2,764, with a pixel size of 1.67 μm. The housing that the camera was placed in allowed the lenslet array to be placed up to 1 mm away from the camera, which is desirable, since the focused

39

configuration of the DPC calls for the distance between the lenslet array and the camera to be adjusted either closer or farther away from the plane at which the image is in focus.
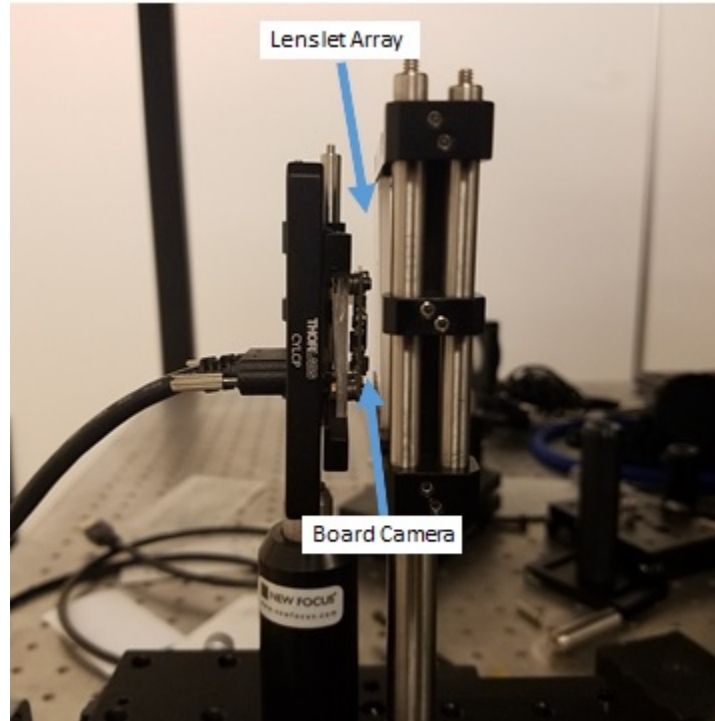
Figure 9. Board camera and lenslet array placement for plenoptic imaging setup.

Figure 16 shows the board camera and lenslet array that were used in order to achieve the imaging conditions required to operate the system as both a conventional and a focused DPC. Due to the small focal length of the lenslet array, a physical setup that allowed both the camera and the lenslet array to be placed in close proximity to each other, within 1 mm, was required. The different a_o values and the corresponding b values that were used for the experiment are shown in the table below.

40

a_o	b
-2 ± 0.025 cm	0.16 ± 0.025 cm
-1 ± 0.025 cm	0.15 ± 0.025 cm
-0.5 ± 0.025 cm	0.12 ± 0.025 cm
-0.3 ± 0.025 cm	0.10 ± 0.025 cm
0 ± 0.025 cm (Conventional)	0.17 ± 0.025 cm
0.3 ± 0.025 cm	0.39 ± 0.025 cm
0.5 ± 0.025 cm	0.25 ± 0.025 cm
1 ± 0.025 cm	0.20 ± 0.025 cm
2 ± 0.025 cm	0.18 ± 0.025 cm

**Table 2. Corresponding a_o and b values used in the experiment for the different DPC setups.**

All the distances calculated in the experiment had a similar uncertainty of ± 0.025 cm associated with them.

41

This section discusses the results obtained from the experiment and explains their overall impact. The outline of this section is as follows. The first section shows a subset of the rendered images from the different setups to show what the rendered images from which the data was being obtained looked like. The following section shows plots of cutoff spatial frequency vs wavelength. These show how the resolving limits of each setup correlate to their setup and shows trends in how the value of a_o affects the overall placement of the curve. This set of data did not show any clear performance improvement from any method. The last set of data discussed is the contrast vs wavelength data obtained from the images. This set of data was obtained from a different set of images than the ones obtained for the cutoff spatial frequency vs wavelength, but they were captured under the same physical setups of the DPC. From this set of data the same trends that were observed for the cutoff spatial frequency on how the value of a_o affects the overall placement of the curve were again observed, but also using this metric led to finding which method performed best and under which circumstances. The effects of a_o and b on the quality of the images is also discussed.

The data collected from the experiment is split into the images collected for each setup, and the images rendered for each setup. There were a total of nine setups that were collected throughout the experiment, and these corresponded to a single setup for the conventional DPC setup, and eight different setups of the focused setup, for eight different values of a_o, which ranged from -2, -1, -0.5, -0.3, 0.3, 0.5, 1, and 2 cm.

42

Figure 17 shows different rendered images at the same wavelength for some of the different setups used in the experiment, the conventional setup, the focused setup, and the images rendered with the RLA. The determination of which was the smallest resolvable element was done by visual inspection.
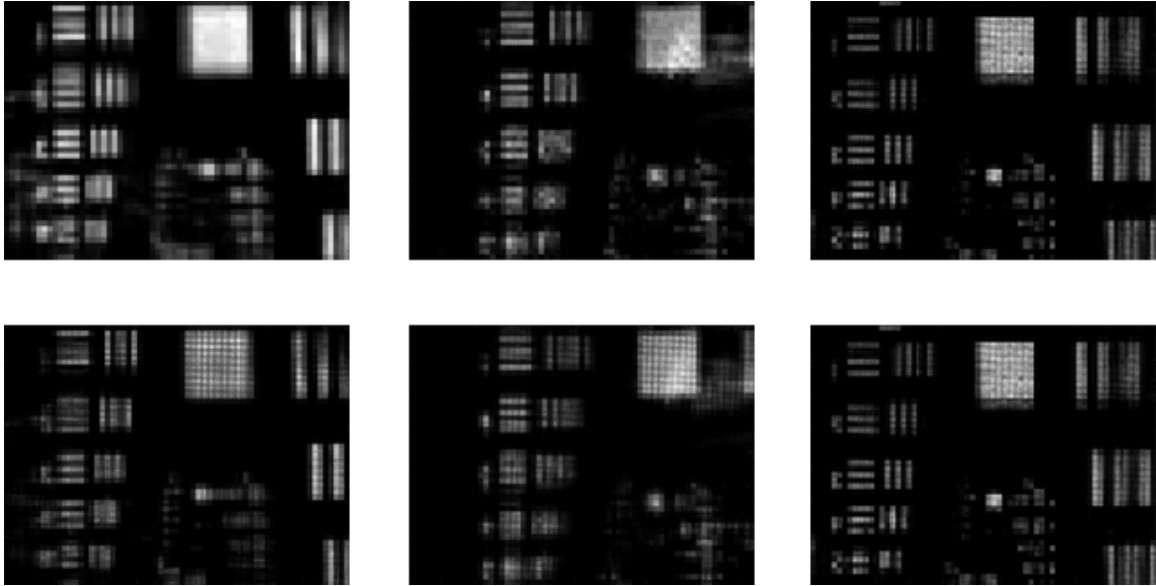
Figure 10. Rendered images at 780 nm from the latest set of images: Conventional (top left), a_o = 1 cm (center top), a_o = -1 cm (top right), RLA conventional (bottom left), RLA a_o = 1 cm (bottom center), RLA a_o = -1 cm (bottom right). For the different images the cutoff spatial frequencies are related to the smallest resolvable element. These smallest resolvable was determined by visual inspection.

The smallest resolvable elements in Figure 17 that were determined were all in group 1 and were elements 3, 2, 4, 3, 2, and 4 respectively for the conventional DPC, the focused DPC at a_o = 1 cm, the focused DPC at a_o = -1 cm, the conventional DPC rendered with the RLA, the focused DPC at a_o = 1 cm rendered with the RLA, and the focused DPC a_o = -1 cm rendered with the RLA. As can be seen in Figure 17 for the case of a_o = -1 cm the smallest resolvable element is the 4 element, whereas for the case of a_o = 1 cm, it is only the 2 element that can be resolved. This reinforces the earlier assertion that was stated

43

along with Figure 13. The assertion was that the system performs better at wavelengths greater than design for negative a_o values because the peak of the M curve occurs at wavelengths less than design for negative a_o, and those are areas where the pixel count is high.
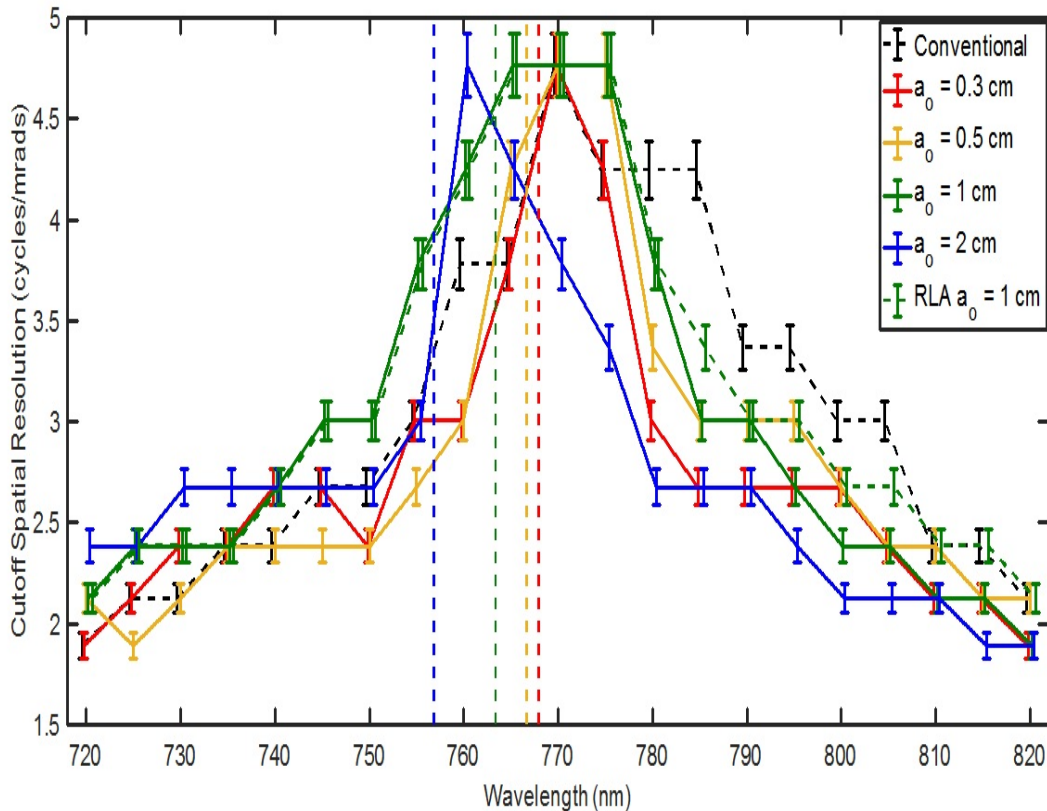
4.1 Cutoff Spatial Resolution

This method of determining the cutoff spatial resolution for each wavelength was carried out for each of the methods that were tested which included: the single conventional DPC, the eight focused DPC setups, the RLA applied to the conventional DPC, the RLA applied setups to two setups of the focused DPC, and images captured with the conventional DPC rendered with the focused algorithm. Figures 18-20 show the cutoff frequencies at different wavelengths for different setups of the DPC, where the cutoff frequencies were calculated according to Equation 6. The plotted cutoff spatial resolution values correspond to the average between the last element to be resolved and the first unresolved element. The reasoning was that the actual cutoff spatial resolution was somewhere in between the last visible element and the next non-visible element.

Figure 18 – 20, show the cutoff spatial resolution vs wavelength for all the methods used to render the images. The first thing to note is that the maximum achieved cutoff spatial resolution, which corresponds to the bars seen in group 1, element 4, is the maximum achieved for most of the rendering methods. This means that no method achieves a better spatial resolution than any other methods. This result means that by the metric of

44

spatial resolution no method is better than the other method. The error bars obtained for the previous plots were done by assuming that the actual cutoff spectral range was somewhere between the element that could be seen and the next smallest element that could not be discerned. It was assumed that probability of being anywhere within that range was equal for any spatial frequency that fell within the range bounded by the two elements, and according to the due to this the error[27] was estimated to be $\pm \frac{\Delta}{\sqrt{3}}$. In this case Δ is the distance from the center of the two spatial frequencies between the two elements under scrutiny, to the next element that could not be resolved.

Figure 11. Cutoff Spatial Resolution vs Wavelength for positive a_o values. For positive a_o values the peak performance occurs at values below the design wavelength (770 nm) and as the positive value of a_o increases the peak performance shifts towards lower wavelengths. The vertical dashed lines

45

correspond to the central wavelengths calculated for each value of a_o. The central wavelength does not line up exactly with the peak performance for each value of a_o, but they are in close proximity. For the line corresponding to $a_o = 1$ cm and the corresponding dashed line, which is for the RLA, the RLA improves upon the maximum cutoff spatial resolution at wavelengths where the focused setup performance starts suffering.

Figure 12. Cutoff Spatial Resolution vs Wavelength for negative a_o values. For negative a_o values the peak performance occurs at values above the design wavelength (770 nm) and as the value of negative value a_o increases the peak performance shifts towards higher wavelengths. The vertical dashed lines correspond to the central wavelengths calculated for each value of a_o. The central wavelength does not line up exactly with the peak performance for each value of a_o, but they are in close proximity. For the line corresponding to $a_o = -1$ cm and the corresponding dashed line, which is for the RLA, the RLA improves upon the maximum cutoff spatial resolution at wavelengths where the focused setup performance starts suffering.
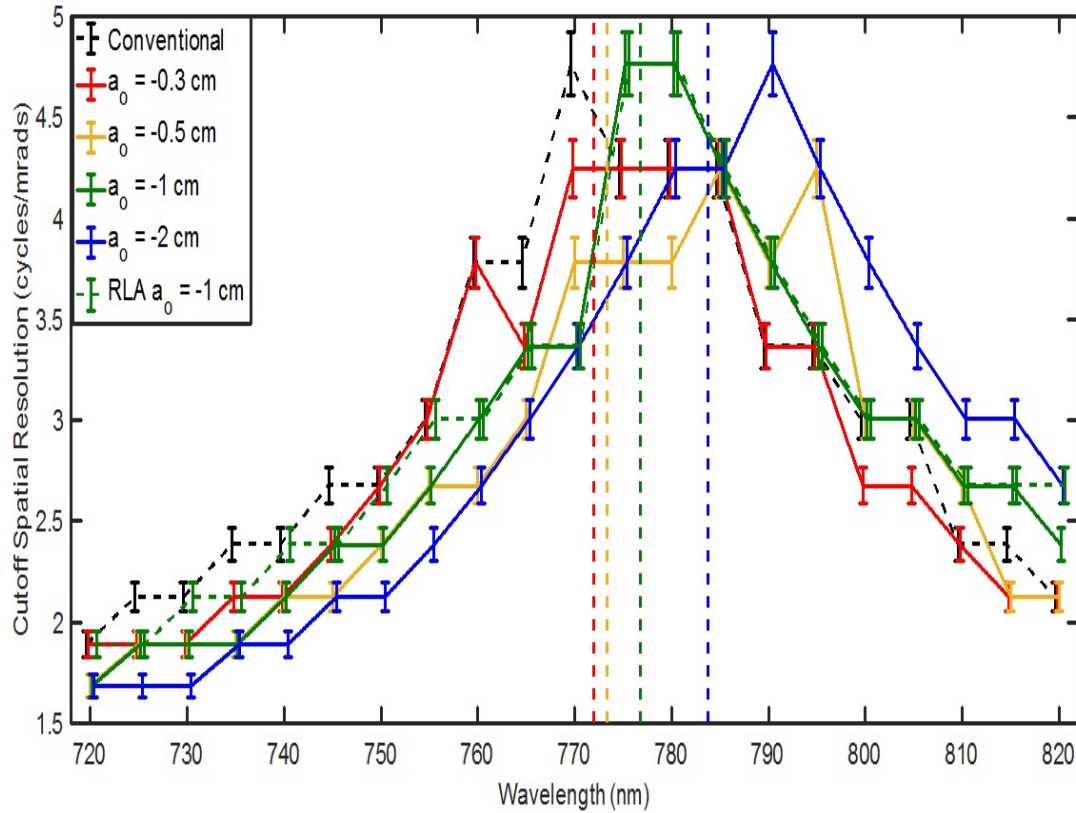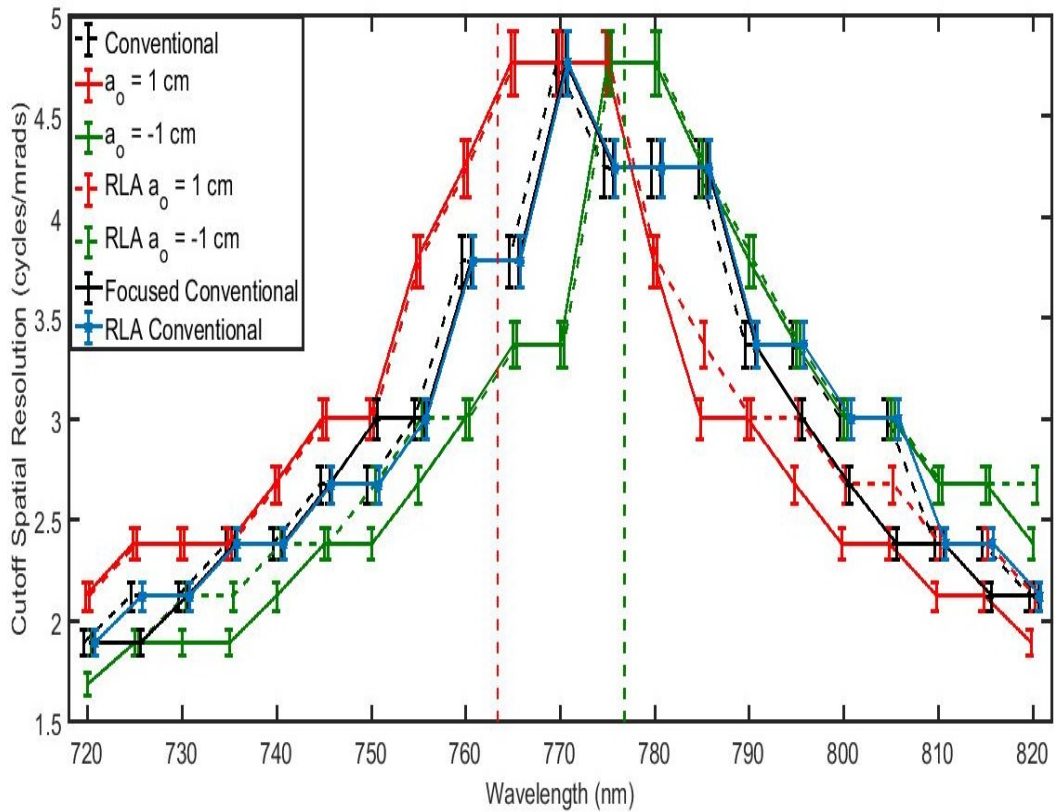
Figure 20. Cutoff Spatial Resolution vs Wavelength comparing both the conventional DPC and the focused DPC to the RLA. The RLA extends the cutoff frequency for both the positive and negative a_o, but it does not improve the cutoff frequency for the conventional algorithm. Using the focusing rendering algorithm with the images captured with the conventional setup decreases the cutoff spatial frequency of the rendered images as compared to the conventional algorithm or the RLA applied to the same pictures. The vertical dashed lines correspond to the central wavelengths calculated for each value of a_o.

It was also seen that the peak performance of each line was directly correlated to its a_o value. For positive values of a_o the peak occurs at wavelengths greater than design, and for negative values of a_o the peak occurs at wavelengths less than design. Again when looking at the dashed vertical lines, which are plotted in accordance to Table 1, and when looking at Figure 13, which shows the M vs λ, it can be seen that the peak performance of each curve lines up with the region in the curve where M peaks. This region where M peaks is related to the area where the pixel count of the rendered images is highest, and it is the

47

area where we get the best performance for all the different systems. It was also seen in Figure 20 that the RLA does improve the performance of the images captured and rendered with the focused DPC at wavelengths far from where the peak performance is supposed to be. This can be explained due to the fact that at these wavelengths far from design, when the image is refocused, some of the detail that was lost due to defocusing is gained back.

4.2 Contrast Calculations

As mentioned another metric by which the images were scrutinized were by their contrast. Equation 7 which is the equation that is used to determine the contrast in the image has two terms that needed to be determined, which were the minimum and maximum intensities. It was mentioned that from each element a total of eight values of contrast were obtained. If any of these eight values fell below a threshold value, which was determined to be $C = 0.10$, then the particular element was determined to be unresolved. This value was determined by noting the result of the contrast calculation on an element which was visually determined to be barely resolved.

In order to determine the intensities used for the contrast methods, three different methods were tried. The first method comprised of looking at the plots of intensity across the rows or columns and from the plots visually determining what the three maximum intensities, and two minimum intensities were. Due to the fact that this method was based entirely on visual inspection, additional methods were approached which leaned less on human inspection. An additional two methods that involved less human decision making

48

were implemented, the first of which was an averaging method. In this method the rows or columns were split into fifths and average across those split areas would be done. Due to the geometry of the bars and rows being imaged, each maximum or minimum should fall within an area that is equivalent to a fifth of the total bar or row, and thus this method was applied. Although in practice this method should produce acceptable results, in reality the results provided by this method were extremely poor. The reason for this was that in actuality the images that were being obtained were not uniform, and thus dividing them into fifths would oftentimes mix an area where there would be a maximum with an area where there would be a minimum. The resulting calculated contrasts from this method provided many results of poor contrast for elements that were clearly resolved, and overall just provided poor contrast results regardless of the element being imaged. The last method applied was an algorithm that would incorporate edge detection, along with prior knowledge of the image being sampled, to determine the areas of maximum and minimum intensities. The results this method produced were very similar to those obtained with via visual inspection. In the end it was this method that was applied throughout the rest of the contrast calculations as it included no human guessing and would provide reasonable results.

From Figures 21 and 22 it can be seen how each method compared to each other and it can be seen from Figures 21 and 22 that the edge detection method is the best method to use since it gives the best results and does not involve any human input. It also shows how poorly the averaging method fared compared to both the visual inspection and edge detection algorithms.
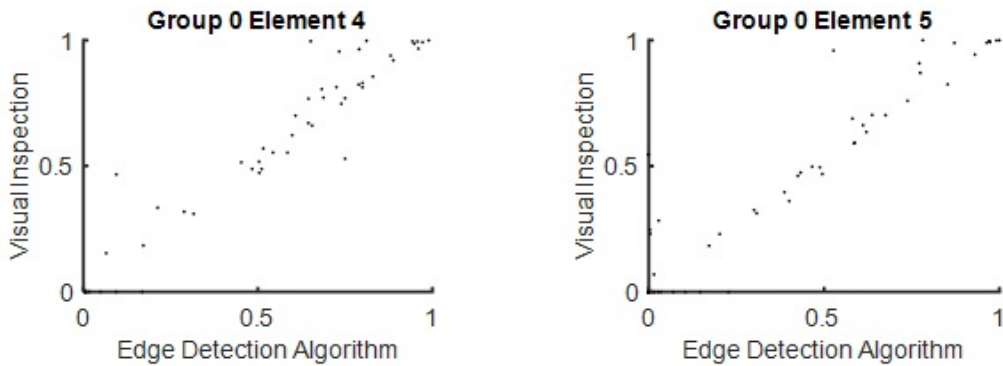
49

Figure 21. Correlation between the mean of the contrast values computed using the visual inspection method to those computed using the edge detection algorithm. Most of the average contrast values that were computed using both methods fall on a line at a 45 degree angle from the origin, indicating strong correlation between the two methods.

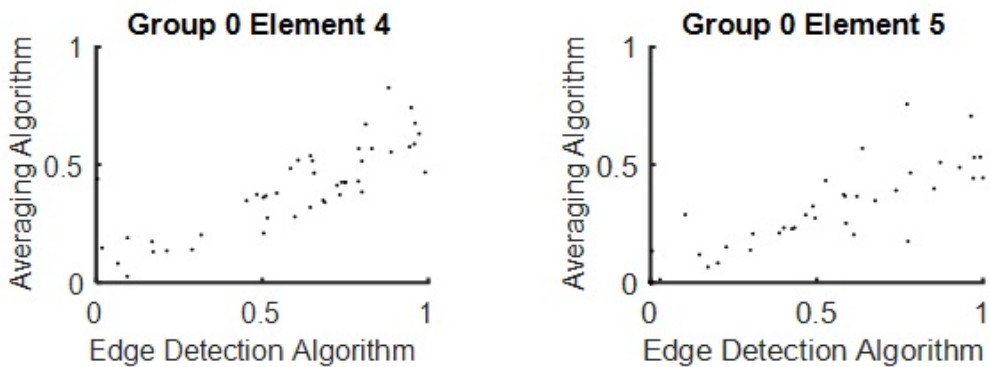**Figure 22. Correlation between the mean of the contrast values computed using the averaging algorithm to those computed using the edge detection algorithm. In this case most of the points do not fall on a line that is 45 degrees from the origin, indicating poor correlation between the results obtained with the Averaging algorithm to those obtained by visual inspection and by the edge detection algorithm.**

What can be seen as well from Figure 21 is how well visual inspection lines up with values calculated without any human input. The cutoff spatial frequencies found for Figures 18-20 were done so by visual inspection, which might raise questions about the validity of the results obtained using such a method. Figure 21 shows that in fact visual inspection does lead to comparable results as those that would be obtained as if the edge detection algorithm was applied to the images. Therefore it can be said that the values obtained in Figures 18-20 are representative of the actual cutoff spatial frequency of the system.

This edge detection method was applied to images captured of the zero group, fourth and fifth elements, from a range of 720-820 nm to obtain a contrast vs wavelength curve. This was done for the single conventional setup, the eight focused plenoptic camera setups mentioned earlier, $a_o = -2, -1, -0.5, -0.3, 0.3, 0.5, 1, 2$ cm, and for images captured with the conventional DPC rendered with the focused, and the RLA, and for images captured at $a_o = -1, 1$ cm rendered with the RLA.

Figures 23-25, show that there is an improvement in performance for the focused DPC over the conventional DPC when measuring it in terms of contrast. As can be seen as well from the dashed lines, the peaks of the contrast curves correspond to the calculated peaks of a_o, and correlate strongly with the curves plotted in Figures 18-20, supporting that cutoff spatial frequency that was estimated by visual inspection. The error bars shown in Figures 23-25 were calculated from the standard deviation of the eight values of contrast obtained from both the rows and columns from each element.

51
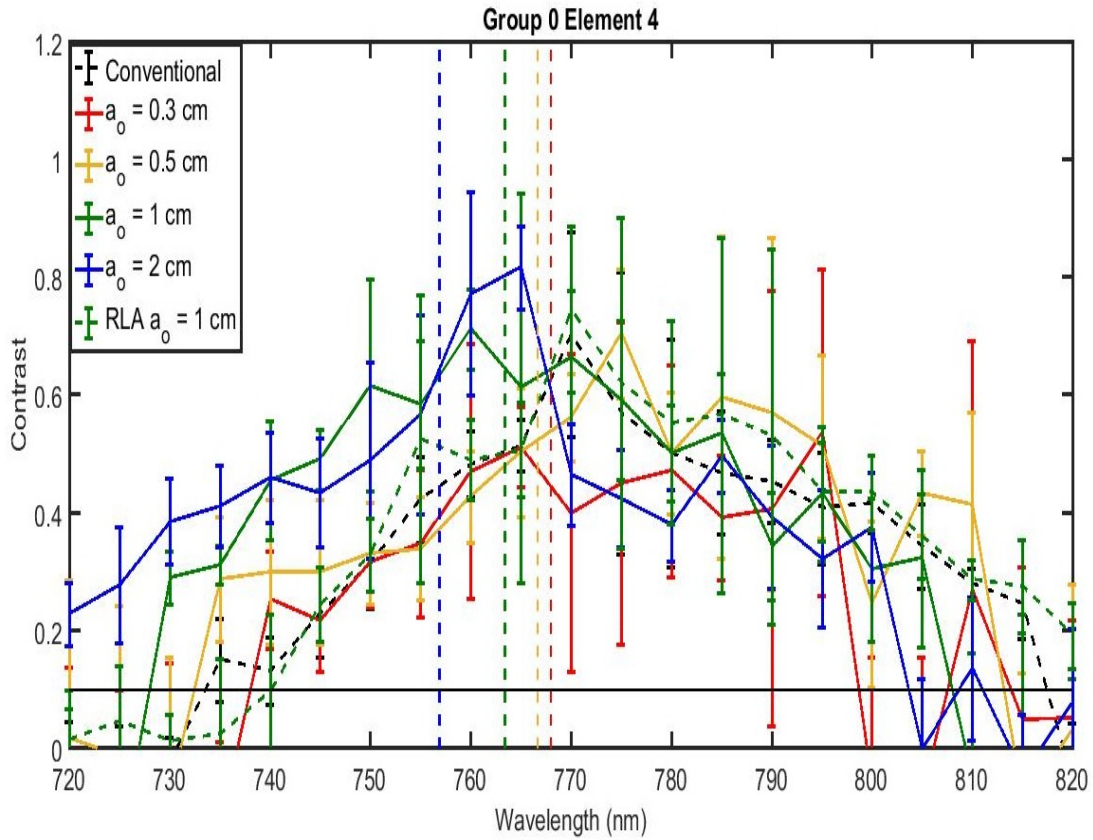
Figure 23. Contrast vs Wavelength for positive a_o values. For positive a_o values the peak performance occurs at values below the design wavelength (770 nm). The contrast of the focused DPC is better than that of the conventional DPC, thus by this metric the focused DPC outperforms the conventional DPC. The vertical dashed lines correspond to the central wavelengths calculated for each value of a_o. The central wavelength does not line up exactly with the peak performance for each value of a_o, but they are close. For the curve corresponding to $a_o = 1$ cm and the corresponding dashed line, which is for the RLA, the RLA improves upon the contrast at values far from the peak from the $a_o = 1$ cm, but does worse than the focused DPC near the peak. For the curve corresponding to $a_o = 0.3$ cm, there is generally poor performance compared to the other curves, and this is due to the large b (0.39 cm) value associated with this value of $a_o = 0.3$ cm.
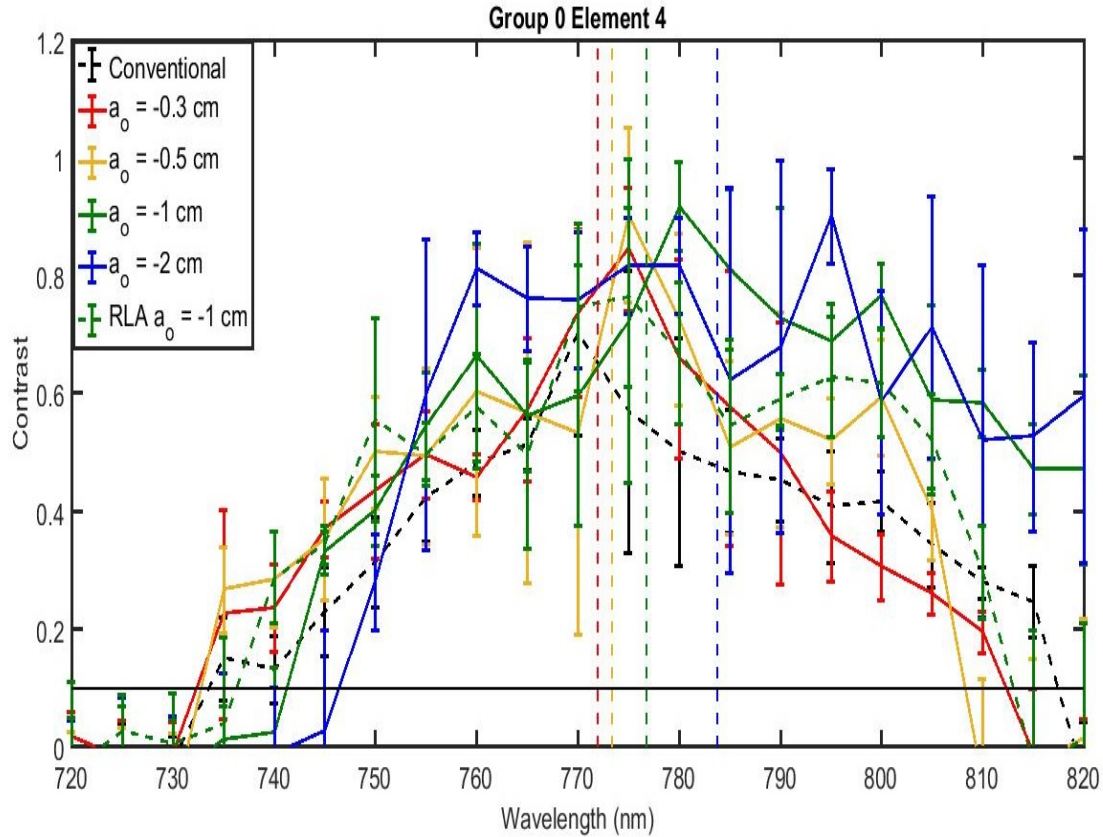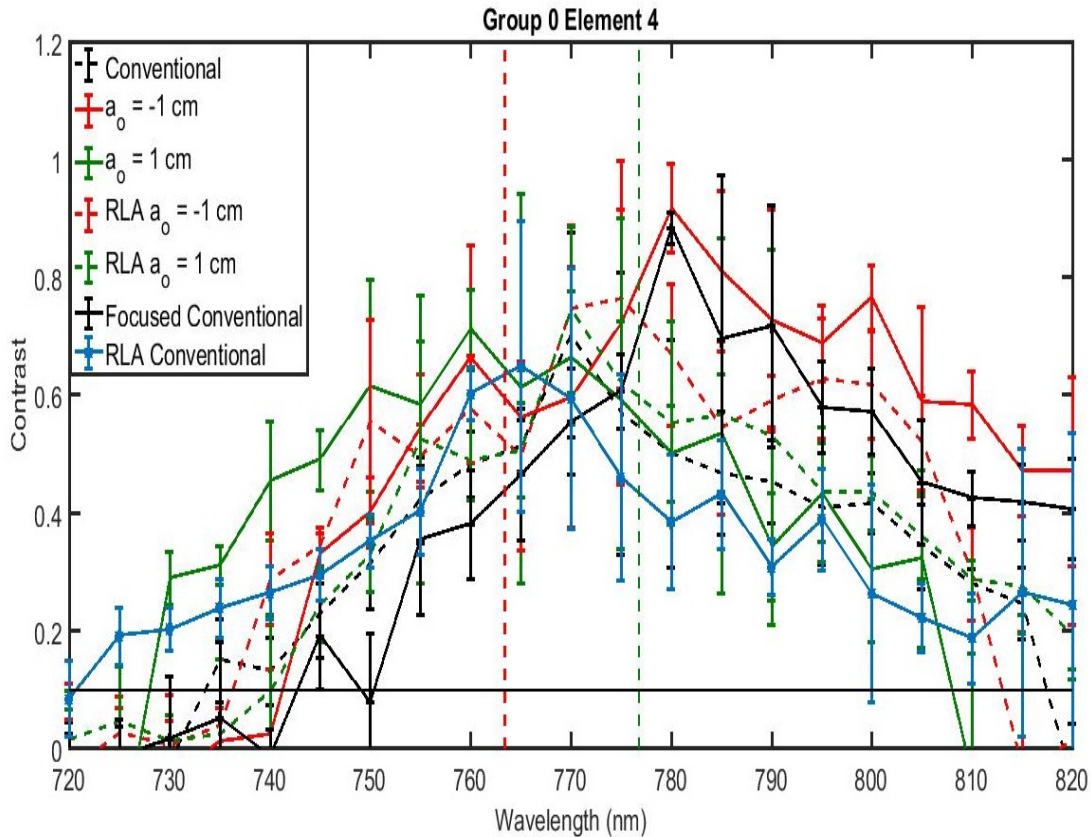
Figure 24. Contrast vs Wavelength for negative a_o values. For negative a_o values the peak performance occurs at values above the design wavelength (770 nm). The contrast of the focused DPC is better than that of the conventional DPC, thus by this metric the focused DPC outperforms the conventional DPC. The vertical dashed lines correspond to the central wavelengths calculated for each value of a_o. The central wavelength does not line up exactly with the peak performance for each value of a_o, but they are close. For the curve corresponding to $a_o = -1$ cm and the corresponding dashed line, which is for the RLA, the RLA improves upon the contrast at values far from the peak from the $a_o = -1$ cm, but does worse than the focused DPC near the peak.

53

Figure 25. Contrast vs Wavelength for comparing both the conventional and focused DPC to the RLA. Both cases of the focused DPC perform the best out of all the other methods. The images captured with the conventional DPC and rendered with the focused DPC and the RLA also improve on the contrast of the conventional DPC in different areas of the curve. The RLA in general improves the contrast in areas where the other rendering methods performance falters.

The reason why elements four and five from group zero were imaged had to do with the large spectral range through which the elements were resolved. For both of the elements, it was possible to reach a wavelength at which the elements became cutoff spatial frequencies, but there was enough of a spectral band where the elements were resolved that it would allow for a contrast vs wavelength curve to be sufficiently populated to understand how these different setups affected the contrast.

54

The effect of the RLA on images captured with the focused and the conventional setups can be seen to improve the contrast in areas where both of the setups' performance starts to falter. Due to the fact that RLA is an algorithm that can be applied to either setup regardless of the conditions used to take the images, the RLA algorithm can be best seen as a tool that supplements the image rendition of both algorithms. In the areas where either algorithm outperforms the RLA, which correlate to where the spectral range peaks for their setup, it seems that it is better to use the original algorithm. But in areas where the setups are far from their design wavelength, where the RLA improves the contrast for both the conventional setup and the focused setup, the RLA would be the better choice in choosing which algorithm to render the images with. The contrast vs wavelengths plots for group zero element five were not included because they show the same trends as those shown in Figures 23-25, but they are included in Appendix A.

4.3 Effect of a_o and b on image quality

Another thing of note to mention is the curve in Figure 23 that belongs to $a_o = 0.3$ cm. As can be seen in Figure 23 this curve shows overall worse performance than every other curve and it leads to the question of what is causing such poor performance. As has been mentioned before, the choice of a_o affects the value of b and with the value of $a_o = 0.3$ cm, the result is $b = 0.39$ cm. But for a similar curve in Figure 24 for $a_o = -0.3$ cm, where $b = 0.10$ cm, the performance does not suffer, so the issue here is not related to the absolute value of a_o, rather it is tied to the value of b. Figure 26 shows the raw images

55

and rendered images that were associated with the two curves, for a_o = -0.3 cm and for

a_o = -0.3 cm and shows what the issue is with this large value of b.
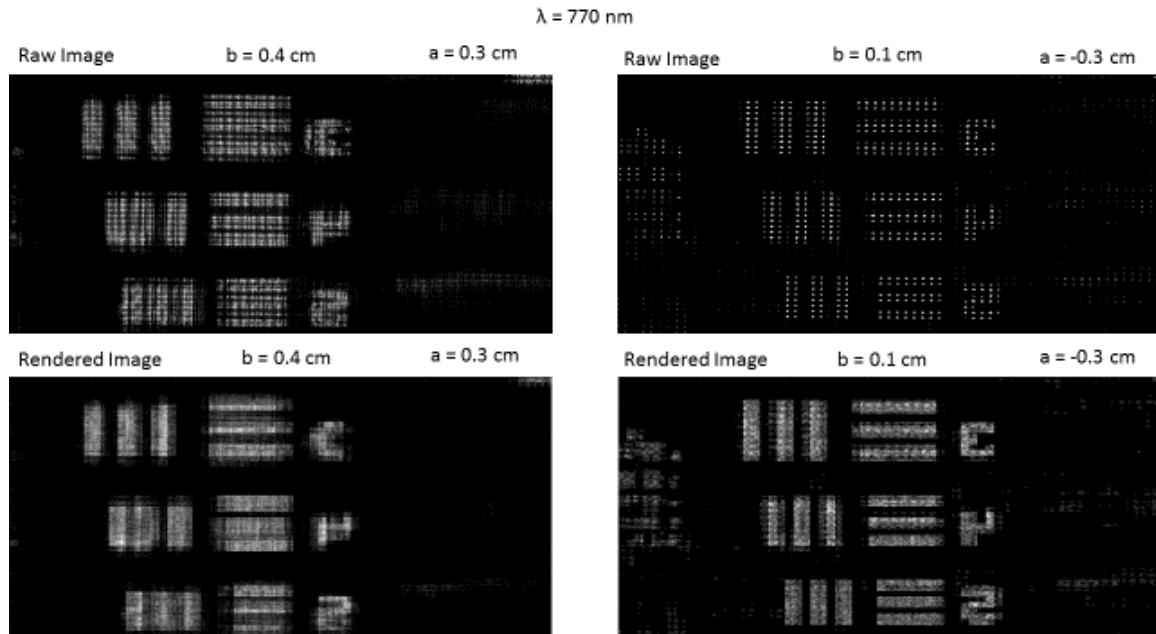
Figure 13. Raw images in the top row, and images rendered after processing with the focused algorithm in the bottom row. There is only a 0.6 cm difference between the placement of the lenslet array between each of the setups, but there is a large difference in the value of b for each a. When b is large compared to the focal length of the lenslet, $b = 0.40\ cm$ compared to $f = .17\ cm$, the raw image has a lot of overlap between the pixels which results in a poorly rendered image. When b is small, $b = 0.10\ cm$, the raw image has no overlap and the resulting image is very well rendered.

As can be seen in Figure 26, for the case when $a_o = 0.3$ cm and $b = 0.40$ cm, the raw image has overlapping pixels between subsequent microlens images, and thus the rendered image is very poorly resolved. The only element that can be clearly discerned from the image if element 3. Whereas the case when $a_o = -0.3$ cm and $b = 0.10$ cm the raw image has no overlapping pixels between subsequent microlens image, and the rendered image is very well resolved. In this image element 5 is fully resolved.

56

This value of b, which is influenced by the choice of a_o and by the focal length of the lenslets f, via the Gaussian Lens Equation, can be used to form threshold values for which a system constructed using the Focused DPC setup. As was noted the value $b = 0.39$ cm proved to be too large and resulted in poor image quality, therefore this can be estimated as being above an upper bound for performance. The next smallest value of b encountered in the experiment was $b = 0.25$ cm, which was the corresponding value for $a_o = 0.5$ cm. From Figure 23 it can be seen that the curve corresponding to $a_o = 0.5$ cm performs as well as the other curves. Therefore it can be stated that this value of $b = 0.25$ cm would be an upper bound in performance for the system. But this value of b is certainly dependent on the physical characteristics of the system, such as the focal length of the system. So in terms of the focal length, this leads to a value of $1.4 f$, as a lower bound for what to set positive a_o. In terms of the smallest value of b that was achieved with the system that corresponded to $a_o =$ -0.3 cm, where $b = 0.10$ cm, which yielded good results. In terms of the focal length this corresponds to $0.6 f$, thus this can be set as the minimum value of negative a_o for which there will still be good performance. This value of $b = 0.10$ cm was also the smallest distance that could be physically achieved with the experimental setup, so that was the smallest value that in practice could be examined. As for the upper bounds of a_o for both negative and positive cases, as a_o increases, b starts approaching f. If b is close enough to f, the resulting case is more similar to a conventional DPC than to a focused DPC. Therefore the upper a_o bound should be related to a value of b that is not equal, or almost equal to f. Therefore an upper bound of $a_o = 12 f$ prevents b from being too close to f. This upper bound of $a_o = 12 f$, was chosen due to the fact that

57

it lined up close to the maximum value in a_o that was tried in the experiment, which was $a_o = \pm 2$ cm. Upper bounds larger than $a_o = 12\,f$, could be possible, but they would need to be tested before it is confirmed that the system would perform as well as with the upper bound of $a_o = 12\,f$.

These bounds lead to the result that a focused DPC should be built within the following constraints of $-12f \leq a_o \leq -0.6\,f$ for negative values of a_o, and $1.4f \leq a_o \leq 12\,f$ for positive values of a_o, in order to obtain a system that performs better than the conventional in terms of contrast for a specific region of interest.

V. Conclusions and Recommendations

In conclusion, the experiment took the two cases of the plenoptic camera, the conventional and the focused, applied then to an imaging system with an FZP, and compared them using two different performance metrics. It was shown that while both systems performed similarly in terms of the spatial frequency, when it came to the contrast the focused DPC outperformed the conventional DPC. It was also seen that the range through which the focused DPC performed the best was directly related to the value of a_o chosen for the system. It was shown that for negative values of a_o the system performed best at values of wavelength greater than the design wavelength, and that for positive values of a_o the system performed best at wavelengths less than the design wavelength. It was also shown that the RLA does in fact help the overall performance of the system. It was shown that for the focused DPC, the RLA will in fact improve the cutoff spatial frequency for values of the wavelength which are far from the central wavelength for the specific case of a_o. It was also shown that the RLA improved the contrast of both the conventional and the focused DPC at values of the wavelength that were far from the central wavelength. Since the RLA is independent of the physical setup of the DPC, it can be applied as a supplemental tool to either the conventional or the focused setup as a means of improving the overall performance of the system at the wavelengths where it would start to falter. The tools and methods studied and developed in this experiment show different ways that imaging techniques can be applied to diffractive optics in order to produce imaging systems with different capabilities, such as the ability to refocus to different spectral bands.

59

Of future interest would be to test this system on a polychromatic scene with different objects in view to further stress the capabilities of the system, and to compare it to modeling data. Improving the imaging algorithms would also benefit future iterations of the system and this could be done by finding methods that could be applied to the different imaging algorithms, the conventional, the focused, and the RLA to improve the quality of the final rendered image.

Bibliography

1. M. T. Eismann, *Hyperspectral Remote Sensing*. (SPIE Press, 2012).

2. H. Kick, V. Tank, and E. Lindermeier, "Impact of scene changes during data acquisition in Fourier spectroscopy", J. Quant. Spectrosc. Radiat. Transfer. **92**(4), 447-455, (2005).

3. L. Palchetti, et al. "Design and mathematical modeling of the spaceborne far infrared Fourier transform spectrometer REFIR experiment," Infrared Phys Techn, **40**(5), 367-377, (1999).

4. F.D. Hallada, A. L. Franz, and M. R. Hawks, "Fresnel zone plate light field spectral imaging,"Opt. Eng. **56**(8), (2017).

5. O. E. Myers, "Studies of transmission zone plates," Am. J. Phys. **19**(6), 359-365, (1951).

6. M. Young, "Zone plates and their aberrations," J. Opt. Soc. Am. **62**(8), 972-976, (1972).

7. F. D. Hallada "The Fresnel Zone Light Field Spectral Imager," M.S. Dissertation, Air Force Institute of Technology, (2017).

8. F.S. Oktem, F. Kamalabadi, and J.M. Davila, "High-Resolution Computational Spectral Imaging with Photon Sieves," IEEE Image Proc. 5122-5126, (2014).

9. M. Hinnrichs and M. Massie, "New approach to imaging spectroscopy using diffractive optics,' Proc. SPIE **3118**, 194-205, (1997).

10. T. Adelson and J. Wang, "Single lens stereo with a plenoptic camera," IEEE Trans. Pattern Anal. Mach. Intell. **99**(2), 99-106 (1992).

11. T. Adelson, and J. Bergen, "The plenoptic function and the elements of early vision," *Computational models of visual processing* (MIT Press, 1991).

12. R. Ng, et al. "Light field photography with a hand-held plenoptic camera," Stanford Tech Report CSTR 2005-02 (2005).

13. R. Ng "Digital Light Field Photography," Ph.D. dissertation, Stanford University, (2006).

14. R. Ng, "Fourier Slice Photography," ACM Trans. Graph., 735-744 (2005).

15. A. Lumsdaine and T. Georgiev, "Full resolution lightfield rendering," Adobe Systems Tech. Rep. (2008).

16. E. Hecht, *Optics*. 5th Ed. (Pearson, 2016).

17. K. Gibbs, "Theories of Light" (School Physics 2017) http://www.schoolphysics.co.uk/age16-19/Wave%20properties/Wave%20properties/text/Theories_of_light/index.html

18. Physics Stack Exchange, "Fresnel Zones – How are they formed", (Stack Exchange, 2017), https://physics.stackexchange.com/questions/89835/fresnel-zones-how-are-they-formed

19. E. Y. Lam "Computational photography with plenoptic camera and light field capture: tutorial," J. Opt. Soc. Am. A **32**(11), 2021-2032 (2015).

20. M. Levoy and P.Hanrahan, "Light field rendering," ACM Trans. Graph., 31-42 (1996).

21. S. J. Gortler, R.Grzeszczuk, R. Szeliski, and M. F. Cohen, "The lumigraph," ACM Trans. Graph., 43-54 (1996).
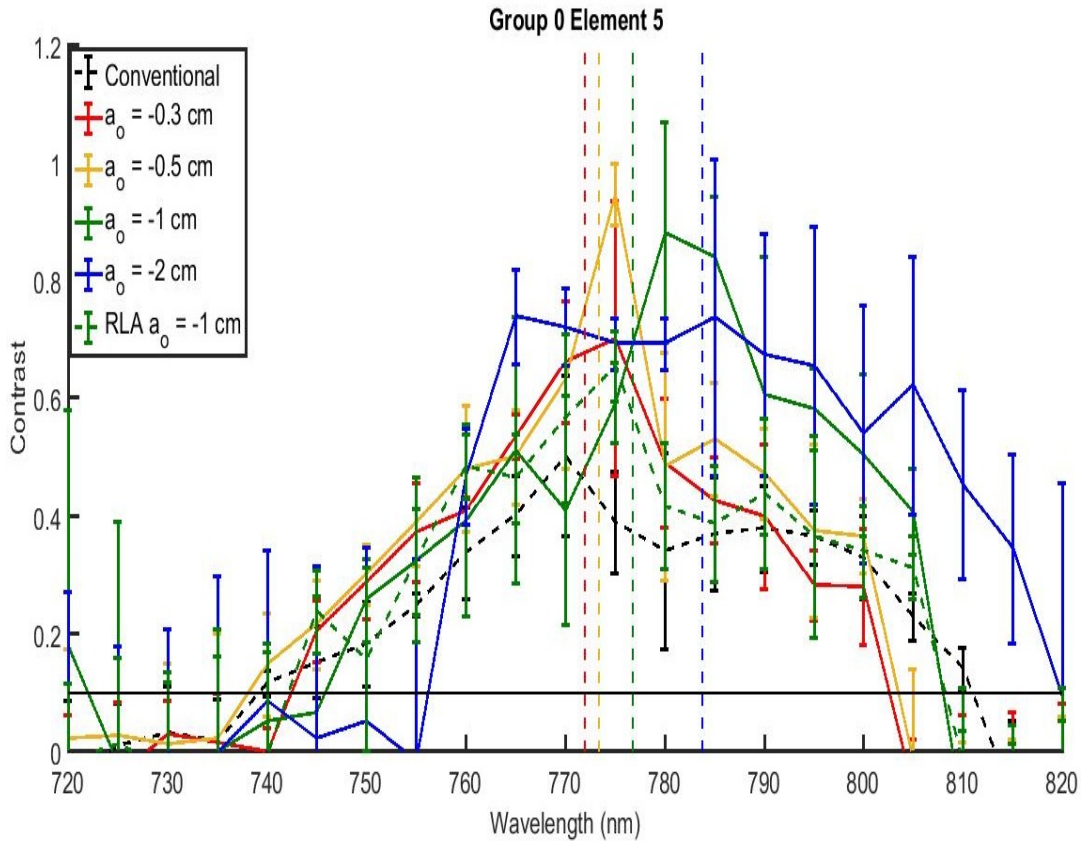
62

22. A. Lumsdaine and T. Georgiev, "The focused plenoptic camera," in IEEE Intl. Conference on Computational Photography, 1-8, (2009).

23. A. Lumsdaine and T. Georgiev, "Focused Plenoptic Camera and Rendering," in J. Electron. Imaging (2010)

24. T. Georgiev, "Computational Methods for Radiance," (2017), http://www.tgeorgiev.net/WSCG2010/Computation.pdf

25. Large Synostic Survey Telescope, "Use of USAF Resolution Chart", (LSSTCorp, 2018), https://dev.lsstcorp.org/trac/.../USAF%201951%20Resolution%20Test%20Target.pdf

26. C. Diaz and R. Peterson, "Characterization of a Ti:Sapphire Laser", in AFIT OENG 616 Report (2017).

27. Joint Committee for Guides in Metrology, *Evaluation of measurement data — Guide to the expression of uncertainty in measurement*. 1st Ed. (JCGM 2008)

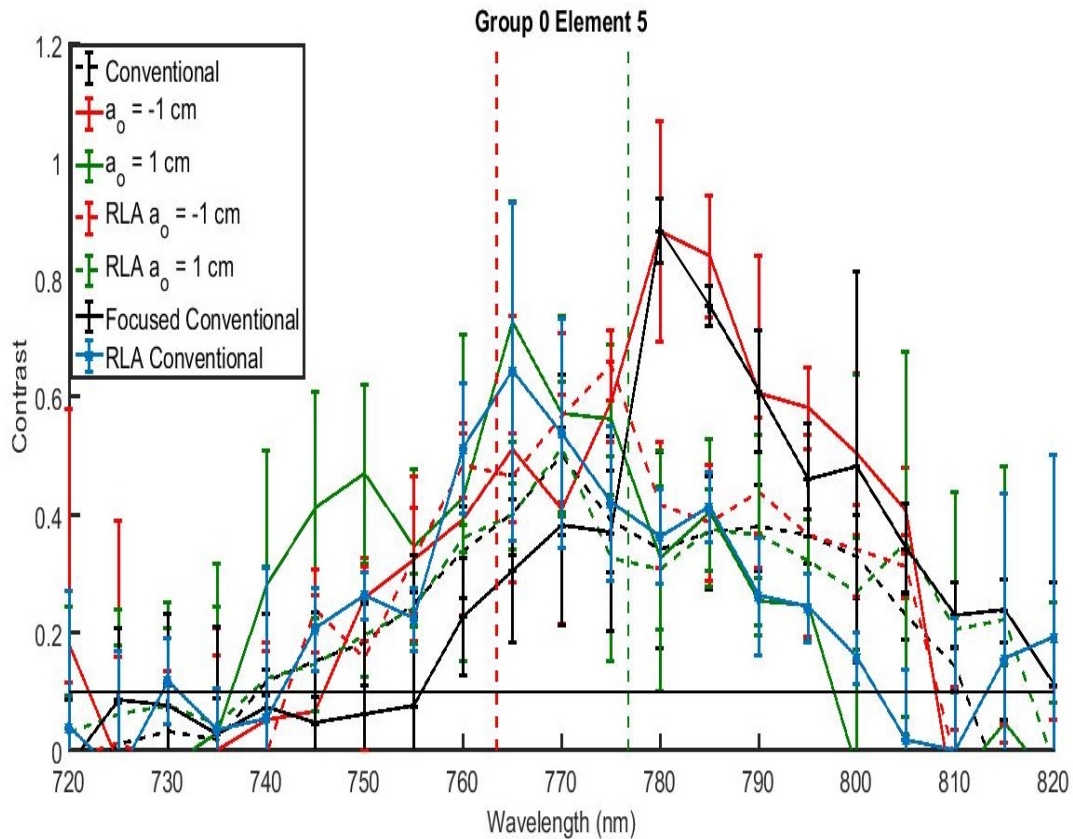## Appendix A. Contrast vs Wavelength Plots of Group 0 Element 5

As was mentioned in the document itself the data of the contrast vs wavelength collected for Group 0 Element 5 was not included in the main document, because it mostly showed exactly what Figures 23-25 did, but for the sake of presenting all the collected data it will be shown here below.
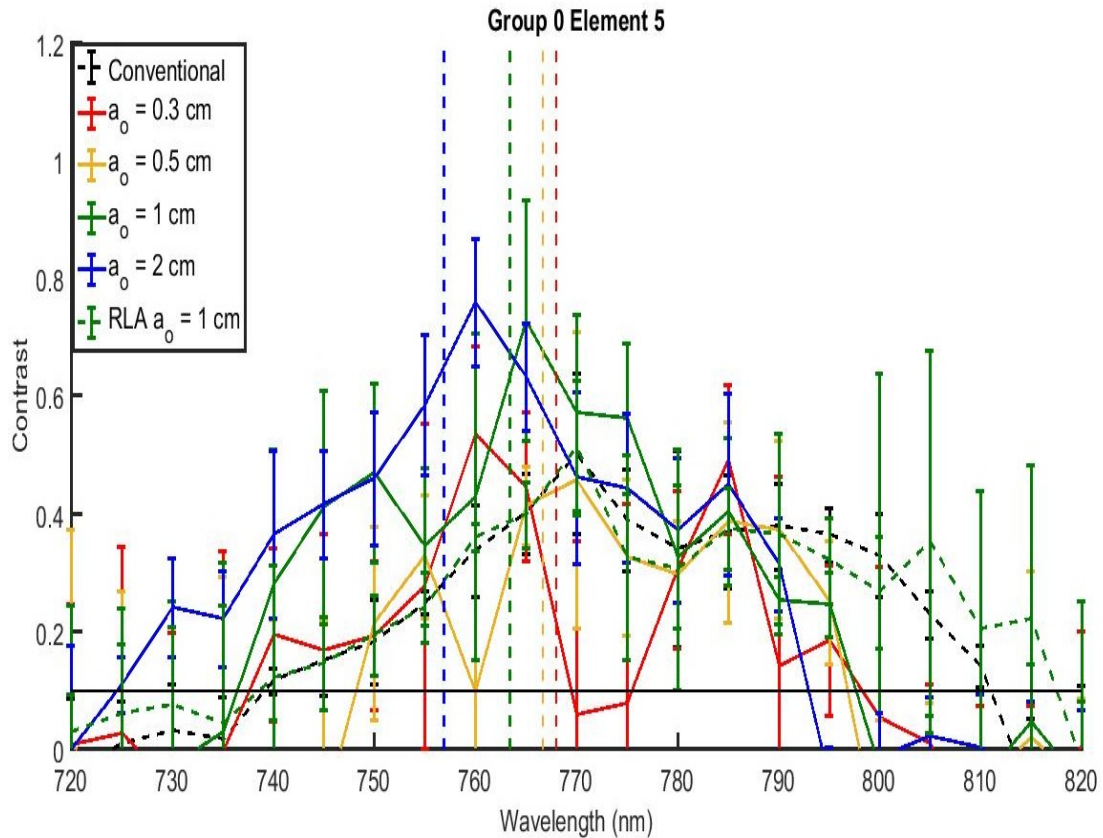
Figure A1. Contrast vs Wavelength for positive a_o values. For positive a_o values the peak performance occurs at values below the design wavelength (770 nm) for Group 0 Element 5. The contrast of the focused DPC is better than that of the conventional DPC, thus by this metric the focused DPC outperforms the conventional DPC. The vertical dashed lines correspond to the central wavelengths calculated for each value of a_o. The central wavelength does not line up exactly with the peak performance for each value of a_o, but they are close. For the curve corresponding to $a_o = 1$ cm and the corresponding dashed line, which is for the RLA, the RLA improves upon the contrast at values far from the peak from the $a_o = 1$ cm, but does worse than the focused DPC near the peak. For the curve corresponding to $a_o = 0.3$ cm, there is generally poor performance compared to the other curves, and this is due to the large b (0.39 cm) value associated with this values of $a_o = 0.3$ cm.

64

Figure A2. Contrast vs Wavelength for negative a_o values. For negative a_o values the peak performance occurs at values above the design wavelength (770 nm) for Group 0 Element 5. The contrast of the focused DPC is better than that of the conventional DPC, thus by this metric the focused DPC outperforms the conventional DPC. The vertical dashed lines correspond to the central wavelengths calculated for each value of a_o. The central wavelength does not line up exactly with the peak performance for each value of a_o, but they are close. For the curve corresponding to $a_o = -1$ cm and the corresponding dashed line, which is for the RLA, the RLA improves upon the contrast at values far from the peak from the $a_o = -1$ cm, but does worse than the focused DPC near the peak.

Figure A3. Contrast vs Wavelength for comparing both the conventional and focused DPC to the RLA for Group 0 Element 5. Both cases of the focused DPC perform the best out of all the other methods. The images captured with the conventional DPC and rendered with the focused DPC and the RLA also improve on the contrast of the conventional DPC in different areas of the curve. The RLA in general improves the contrast in areas where the other rendering methods performance falters.

REPORT DOCUMENTATION PAGE

The public reporting burden for this collection of information is estimated to average 1 hour per response, including the time for reviewing instructions, searching existing data sources, gathering and maintaining the data needed, and completing and reviewing the collection of information. Send comments regarding this burden estimate or any other aspect of the collection of information, including suggestions for reducing this burden to Department of Defense, Washington Headquarters Services, Directorate for Information Operations and Reports (0704-0188), 1215 Jefferson Davis Highway, Suite 1204, Arlington, VA 22202-4302. Respondents should be aware that notwithstanding any other provision of law, no person shall be subject to an penalty for failing to comply with a collection of information if it does not display a currently valid OMB control number.
PLEASE DO NOT RETURN YOUR FORM TO THE ABOVE ADDRESS.

1. REPORT DATE *(DD-MM-YYYY)* 22-03-2018	2. REPORT TYPE Master's Thesis	3. DATES COVERED *(From – To)* September 2017 – March 2018

TITLE AND SUBTITLE **SPATIAL RESOLUTION AND CONTRAST OF A FOCUSED DIFFRACTIVE PLENOPTIC CAMERA**	5a. CONTRACT NUMBER
	5b. GRANT NUMBER
	5c. PROGRAM ELEMENT NUMBER
6. AUTHOR(S) Diaz, Carlos D., Captain, USAF	5d. PROJECT NUMBER
	5e. TASK NUMBER
	5f. WORK UNIT NUMBER

7. PERFORMING ORGANIZATION NAMES(S) AND ADDRESS(S) Air Force Institute of Technology Graduate School of Engineering and Management (AFIT/ENP) 2950 Hobson Way, Building 640 WPAFB OH 45433-8865	8. PERFORMING ORGANIZATION REPORT NUMBER AFIT-ENP-MS-18-M-077
9. SPONSORING/MONITORING AGENCY NAME(S) AND ADDRESS(ES) Intentionally Left Blank	10. SPONSOR/MONITOR'S ACRONYM(S)
	11. SPONSOR/MONITOR'S REPORT NUMBER(S)

12. DISTRIBUTION/AVAILABILITY STATEMENT
  DISTRUBTION STATEMENT A. APPROVED FOR PUBLIC RELEASE; DISTRIBUTION UNLIMITED.

13. SUPPLEMENTARY NOTES
This material is declared a work of the U.S. Government and is not subject to copyright protection in the United States.

14. ABSTRACT
The conventional Diffractive Plenoptic Camera (DPC) was developed as a system that would capture the spectral and spatial information of a scene in one snapshot. The conventional DPC couples a diffractive optic with plenoptic camera designs that provide snapshot spectral imaging capabilities but produce rendered images with low pixel count. A modified setup of the conventional DPC, the focused DPC, and a modified imaging algorithm, the refocused light field algorithm, were built and tested for the first time, and compared to the conventional DPC as methods that would increase the pixel count and improve rendered image quality. The focused DPC achieved the same cutoff spatial frequency, improved the contrast in comparison to the conventional DPC, and it shifted the wavelength at which peak performance occurred. The refocused light field algorithm improved the cutoff spatial frequency of the focused DPC, and improved the contrast of both the conventional and the focused DPC setups at wavelengths far from peak performance. The focused DPC was demonstrated as a system that improved performance as compared to the conventional DPC, and the refocused light field algorithm was demonstrated as a tool that could extend the imaging capabilities of both DPC setups.

15. SUBJECT TERMS
Spectral Imaging, Plenoptic Camera, Diffractive Optics, Focused Plenoptic Camera, Image rendering algorithms, Fresnel Zone Plate

16. SECURITY CLASSIFICATION OF:			17. LIMITATION OF ABSTRACT	18. NUMBER OF PAGES	19a. NAME OF RESPONSIBLE PERSON Lt Col Anthony L Franz, AFIT/ENP
a. REPORT	b. ABSTRACT	c. THIS PAGE	UU	67	19b. TELEPHONE NUMBER *(Include area code)* (937) 255-3636 x4429 (Anthony.franz@afit.edu)
U	U	U			